UAV-Based Geomorphological Evolution of the Terminus Area of the Hailuogou Glacier, Southeastern Tibetan Plateau between 2017 and 2020

Shuyang Xu[a], Ping Fu[a*], Duncan Quincey[b], Meili Feng[a], Stuart Marsh[c], Qiao Liu[d],

a School of Geographical Sciences and Geospatial and Geohazards Research Group, Faculty of Science and Engineering, University of Nottingham Ningbo China, Ningbo, China

b School of Geography and water@leeds, University of Leeds, West Yorkshire, England, U.K

c Nottingham Geospatial Institute, Faculty of Engineering, University of Nottingham, Nottingham NG7 2TU, U.K

d Institute of Mountain Hazards and Environment, Chinese Academy of Sciences, Chengdu, China

*Author to whom correspondence should be addressed.

Highlights:

- Recent geomorphological changes for Hailuogou Glacier terminus area are analyzed using SfM-MVS workflow with UAV images from September 2017 to November 2020.
- The terminal area not affected by collapse events retreated 132.1 m, whereas the area subject to collapse events retreated 236.4 m.
- The ice volume reduction for the observed areas is $184.61 \pm 10.32 \times 10^4$ m^3, and ~28% was attributed to ice collapse.
- The evolution of the HLG Glacier terminus will continue to be dominated by the frontal ice collapse

Abstract

Hailuogou (HLG) Glacier, a rapidly receding temperate glacier in the southeastern Tibetan Plateau, has been observed to lose mass partly through ice frontal mechanical ablation (i.e., ice collapse). These events are difficult to monitor and quantify due to their small scale and frequent nature. However, recent developments in Uncrewed Aerial Vehicles (UAV) have provided a possible approach to track their spatiotemporal variation and their impact on the geomorphological evolution of the glacier terminus area. Here, we present analysis from UAV surveys conducted over eight field campaigns to the HLG Glacier, providing evidence of glacier change between October 2017 and November 2020. Structure from Motion with Multi-View Stereo (SfM-MVS) was applied to produce multi-temporal Digital Surface Models (DSMs) and orthophoto mosaics, from which geomorphological maps and DEMs of Difference (DoDs) were derived to quantify glacier changes. These analyses reveal that at the margins of the glacier terminus retreated 132.1 m over the period of analysis, and that in the area specifically affected by collapsing (i.e., the glacier collapsed terminus), it retreated 236.4 m. Overall the volume lost in the terminal area was of the order of $184.61 \pm 10.32 \times 10^4$ m^3, within which the volume change due to observed collapsing events comprises approximately 28%. We show that ice volume changes at the terminus due to a single ice collapse event may exceed the interannual level of volume change, and the daily volume of ice loss due to ice calving exceeds the seasonal and interannual level by a factor of ~ 2.5 and 4. Our results suggest that the evolution of the HLG Glacier terminus is dominantly controlled by the frontal ice-water interactions. If the future evolution of glaciers such as HLG Glacier is to be robustly predicted, the contribution of mechanical ablation should be accounted for by numerical models.

Keywords: Hailuogou Glacier, Frontal ice collapsing, Uncrewed aerial vehicles, Geomorphological evolution

1. Introduction

Hailuogou (HLG; Randolph Glacier Inventory ID: RGI60-15.07886) Glacier is the longest glacier in the Glacier Park located on the eastern slope of Mt. Gongga (7556 m above sea level), southeastern Tibetan Plateau (SE TP). It is a partly debris-covered temperate glacier and is the main source of the River of Moxi, a branch of Dadu and Yangtze River. HLG Glacier has been reported to be receding rapidly in a number of studies, which commonly associate the retreat with warming (e.g., Ding et al., 2006; Pan et al., 2012; Wu et al., 2020; Yang et al., 2016). However, apart from processes of ice loss related directly to changes in temperature (i.e., mass loss due to melt), the mechanical ablation of glaciers can also play an important role in contributing to ice mass changes (Benn and Åström, 2018). Mechanical ablation can be described as the process by which ice fractures from the host glacier, most commonly as a consequence of ice-marginal water-glacier interactions (Falatkova et al., 2019; Haresign, 2004; Sakai, 2012; Sakai and Fujita, 2010). The understanding of mechanical ablation and its contribution to overall ice loss has been hindered because it is difficult to track mechanical ablation by commonly-available satellite-based remote sensing datasets, owning to their small-scale but unpredictable natures. Fortunately, the use of imagery acquired by Uncrewed Aerial Vehicles (UAV) can be acquired with much greater frequency, at lower altitudes, to capture these fine-scale changes. Structure from Motion with Multi-View Stereo (hereon, SfM-MVS) photogrammetry has been well developed in connection with the UAV technology to reconstruct the three-dimensional glacier surface through time (Bash et al., 2018; Chandler et al., 2018; Rossini et al., 2018a).

It is generally agreed that mechanical ablation can amplify ice loss when compared to glaciers without such processes, leading to the glacier (e.g., no lake-terminating glaciers) behavior that is partly decoupled from climatic drivers (Carrivick and Tweed, 2013a). Recently, efforts to characterize and quantify the mechanical ablation for mountain glaciers have been carried out on lake-terminating glaciers and their proglacial lakes (e.g. Ashraf et al., 2014; Carrivick and Tweed, 2013; Haresign, 2004; King et al., 2018, 2019; Liu et al., 2020; Sakai, 2012; Sakai et al., 2009). However, similar rates of mechanical ablation may also be observed for some land-terminating monsoonal temperate glaciers in the SE TP, such as HLG

Glacier, which exhibits ~13° of surface gradient in the lower glacier tongue (Zhong et al., 2021). They have been observed in the field predominantly as collapse events, probably influenced by the ablation induced by the intensive water-glacier interactions along the subglacial channels, around the subglacial outlet (i.e., the intersection between the proglacial river and the glacier terminus), and within the subglacial conduits around the glacier terminus (i.e., the conduit's roof)

Ice collapsing and calving events take place rapidly, meaning their frequency and magnitude can be difficult to ascertain (Haresign, 2004). Though current satellite-based remote sensing technologies have provided multiple options for glacier change monitoring, using optical sensors (e.g., Landsat, ASTER and Sentinel-2), microwave sensors (e.g., Sentinel-1) and gravity sensors (e.g., GRACE), (Berthier and Toutin, 2008; Bishop et al., 2007; Chen et al., 2018; Kääb et al., 2016; Li et al., 2008; Strozzi et al., 2002), it is difficult to quantify fine-scale changes using these coarse resolution data sources. Although field investigations can be challenging (e.g., high lateral relief, complex terrain, poor signal transmission, unsteady weather, etc.), several previous works have been successful in glacier monitoring using low-cost consumer-grade UAVs (e.g., Immerzeel et al., 2014; Fugazza et al., 2018; Rossini et al., 2018a; Yang et al., 2020; Karimi et al., 2021; Fu et al., 2021). For example, to track the modification of glacial geomorphological features over short timespans (Fugazza et al., 2018), to characterize the sub-annual and annual formation of ice-marginal landforms (Rossini et al., 2018a), and to quantify glacier volume changes and the dominant melting processes (Di Rita et al., 2020).

Land-terminating mountain glaciers in the SE TP, such as HLG Glacier, are undergoing remarkable recessions in recent decades (Li et al., 2009, 2010; Liu et al., 2010; Lu and Gao, 1992; Zhang et al., 2011). In this study, we aimed to quantify the extent to which this enhanced recession could be attributed to seasonally enhanced ice-marginal water-glacier interactions (i.e., during summer period), and a consequent increase in mechanical ablation activity. With the employment of UAV-captured imagery over the HLG Glacier from October 2017 to November 2020, and 3D surface reconstruction technology, we sought to achieve the following objectives:

1. to characterize the morphological evolution of the glacier terminus due to mechanical ablation (i.e., collapse activity) using fine spatial resolution images from UAV, and;

2. to quantify volumetric ice loss across the terminus area owing to mechanical ablation as opposed to other ablation processes (i.e., melt and sublimation).

2. Study area

HLG Glacier is the longest temperate glacier located at the eastern slope of Mt. Gongga (29.6°N, 101.9°E), which is the highest mountain on the southeastern edge of the Tibetan Plateau (Fig.1; Li et al., 2010). Mt. Gongga (i.e. Minya Konga) has the highest peak reaching 7556 m above sea level (a.s.l) and it is one of the most extensively glaciated regions in the SE TP (Zhang et al., 2010, 2012). There are 74 glaciers located in the region of Mt. Gongga (Liu and Zhang, 2017), but only five exceed 10 km in length (Li et al., 2010). The temperate glaciers in these regions are known for high mass turnover and high ice flow velocity due to high ablation and high accumulation simultaneously in summer (Aizen and Aizen, 1994; Liu et al., 2018; Su and Shi, 2000). The climate of HLG catchment is characterized by southwest (India and Bengal monsoons) and southeast monsoons, which dominate during the summer (wet season), and by the westerly circulation, which dominates during the winter (dry season) (Li et al., 2010; Zhang et al., 2010).

Within the HLG catchment (area of ~ 80.5 km^2), there are seven contemporary glaciers with total areal coverage of 36.44 km^2 (Zhang et al., 2012; Xu and Yi, 2017). HLG Glacier is the largest glacier in the HLG catchment with a length of about 13 km, 25 km^2 in area, and covering an altitude range of 2901 – 7556 m a.s.l (Li et al., 2010; Zhang et al., 2010; Liu et al., 2010; Sun et al., 2018; Wang et al., 2013). Below the ice fall, the ablation area is about 2 km^2 and most of the glacier tongue is covered by supraglacial debris due to processes of frost weathering and rock avalanches (Zhang et al., 2011, 2012). The Equilibrium Line Altitude (ELA) of HLG Glacier is about 5273 m a.s.l in 2009 and the ELA for most glaciers in this region ranges from 4200 to 5200 m a.s.l (Li et al., 2010; Zhang et al., 2018). The thickness of supraglacial debris increases progressively from the icefall down to the terminus, where it has been measured at 0.6 m according to Zhang et al. (2010).

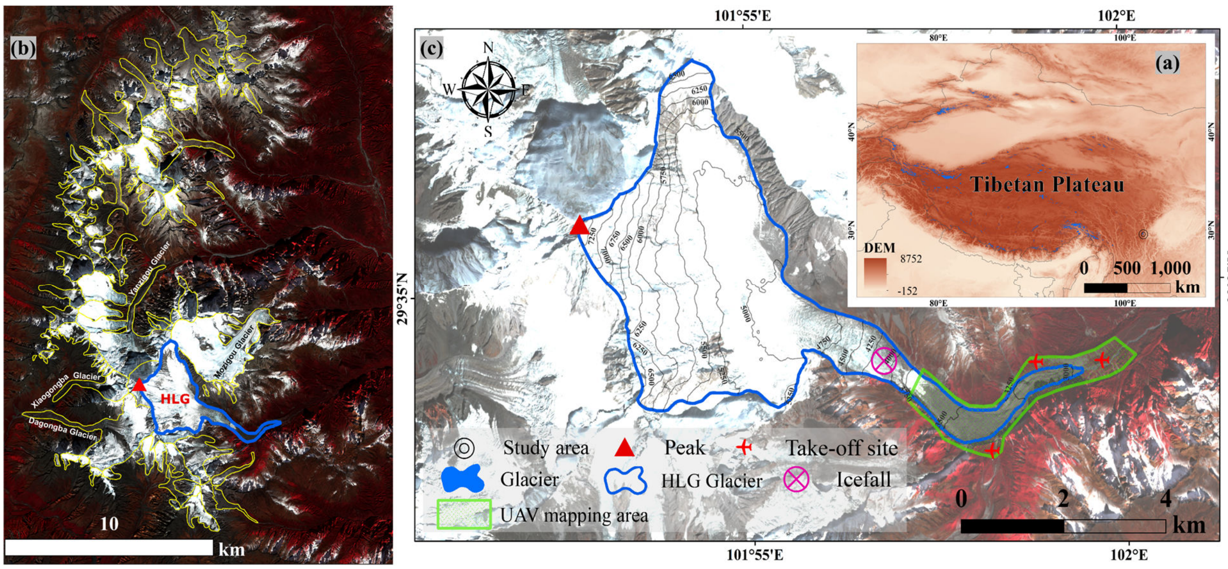

Fig 1. Site plan showing the location of Tibetan Plateau and within that, the location of our study area, and the location of UAV flights. (a) An illustration of the rough range of the Tibetan Plateau and the locations of the study area. The glacier outline is from the Second Glacier Inventory of China version 1 (Liu et al., 2014). The terrain background was extracted from GTOPO30 (~ 1km resolution) (USGS, 1997). (b) Glaciers of the Gongga Mountain range are highlighted in yellow, and the extent of the HLG Glacier is outlined in blue. The background image is a false-color composite of Sentinel 2A of 10th November 2020 (same for the subfigure c). (c) The extent of UAV mapping in the HLG Glacier valley. The green polygon shows the UAV mapping area, ranging from the icefall to periglacial forest.

The terminus of HLG Glacier has retreated about 2 km since the 1930s (Liu and Zhang, 2017). HLG Glacier retreated around 1.15 km from 1966 to 2010 with an annual retreat rate of 25 to 30 m a^{-1} (Zhang et al., 2015). The mean thinning rate of the HLG Glacier tongue was 33.9 ± 11.2 m between 1989 and 2008, which equates to around 26% of the ice thickness recorded in 1990 (~130 m) (Liu and Zhang, 2017). Based on repeat stake surveying, glacier velocity in the ablation zone decreased by about 31% between 1981 and 2008, indicating a reduction in mass turnover (Zhang et al., 2015, 2010). Moreover, the area of HLG Glacier has reduced to 25.3 km^2 from 26.1 km^2 between 1966 and 2009 (Pan et al., 2012), and the annual average thinning rate is 0.90±0.45 m a^{-1} (Zhang et al., 2016) (Tab. 1). Based on recent research, the area of the HLG Glacier tongue has declined from 2.65 ± 0.01 to 1.95 ± 0.02 km^2 between 2002 to 2020, and the retreat rate of the glacier terminus was about 6 ± 0.44 m a^{-1} and $\sim 54 \pm 0.39$ m a^{-1} during the periods 2002 to 2016 and 2016 to 2020, respectively (Zhong et al., 2021).

Table.1 HLG Glacier changes from 1966 to 2010 (adapted from Zhang et al., 2015)

Characteristics of Changes	1966-1989	1989-2010	Total
Terminus retreat (m)	743	410	1153
Area changes (km^2)	0.3	0.5	0.8
Elevation changes (m)	15.1 ± 22.8	24.1 ± 11.0	39.2 ± 20.0
Volume changes ($10^{-3}km^{-3}$)	-		-1.71

3. Data and Methods

The glacial geomorphic features and the 3D surface of the glacier terminus were mapped and reconstructed based on the high-resolution UAV images captured from field trips. From 2017 to 2020, we undertook eight field trips to HLG Glacier, most of which fell within ablation months (June to November). Owing to the flying capacity of the UAV and the unsteady weather conditions, the area covered, and the flight altitude of mapping varied between campaigns (Table 2).

Table 2. General Information about products generated from SfM-MVS workflow

No.	Date (y/m/d)	Numbers of photo	DSM (m/px)	Ortho-images (m/px)	Georeferencing errors (RMSE; cm)
1	2017/10/17	2463	0.09	0.022	15.47
2	2017/12/04	1284	0.16	0.040	21.45
3	2018/06/30	1066	0.27	0.066	25.49
4	2018/10/28	4850	0.31	0.079	31.37
5	2019/10/03	3013	0.35	0.087	19.36
6	2020/09/05	898	0.07	0.037	35.51
7	2020/09/10	282	0.11	0.053	32.63
8	2020/11/05	315	0.18	0.054	33.82

3.1 Data source

Nearly 14,000 still images were acquired, and more than 3600 images were extracted from aerial videos. We implemented the UAV mapping missions covering the part or whole glacier tongue by different piloting strategies mainly due to the weather conditions (i.e., heavy cloud or wind) in the HLG glacier valley. In this paper, we only focus on the terminus region of the glacier tongue.

a) UAV Platform

We used a consumer-grade quadcopter, DJI Mavic Pro, for implementing the fieldwork, known for high-performance in high mountain regions, as well as being compact size, having good handling ability and relatively low cost for conducting high-resolution landform investigations (Hendrickx et al., 2019; Stucky de Quay et al., 2019). The positioning systems are an integrated GNSS system with BDS, GPS and GLONASS. The onboard camera is a 12.71-megapixel sensor with the ability to capture JPEG format or RAW images in the visible light range. The onboard camera is an FC220 with a focal length of 4.73 mm.

b) Drone Sorties Planning and UAV Images Capturing

We used Pix4D capture to plan flight missions in detail and execute missions automatically. The flight parameters can be set up in advance such as camera posture, overlapping parameters and drone speed. However, it is not suitable to conduct a fully automatic flight mission for the entire ablation zone of the HLG glacier due to its high relief and frequently unstable weather conditions. We therefore flew manually for parts of the ablation zone to ensure sufficient image overlap and quantity. Specifically, firstly we adopted the terrain-following flight mission strategy for the UAV mapping as the elevation of the HLG Glacier tongue is ranging from ~2900 to 3500 m a.s.l. In other words, the mapping area was covered separately with four gridded flight paths with variable flying heights to maintain relatively constant ground resolutions. The onboard camera of the UAV was pre-set with nadir viewing angle to obtain orthophotos with a longitudinal and side overlapping of 70% and 80%, respectively. The drone was not able to capture images beyond the icefall (red triangle in Fig. 1) given its altitude, so the mapping area covers from icefall to glacier terminus and part of the periglacial forest (as shown by the yellow grid in Fig. 1).

c) Ground control point collection

We collected six sets of Ground Control Points (GCPs; Fig. 2) during the field trip of 2018. These GCPs are distributed around the proglacial zone of the HLG Glacier since the glacier surface is highly unstable and points are often difficult to locate in aerial imagery. We aimed to identify features from artificial and stable constructions, such as road junctions, using two GNSS geodetic receivers simultaneously (i.e., one was set as the master station and the other is the rover). The master station was installed on the rooftop of a hotel in the HLG Glacier Park to acquire the long-time observation needed for a static referencing point. The rover measurement was conducted by occupying the GCPs for at least 2 mins during periods of comprehensive satellite coverage, and the resulting coordinates were post-processed to export the GCPs.

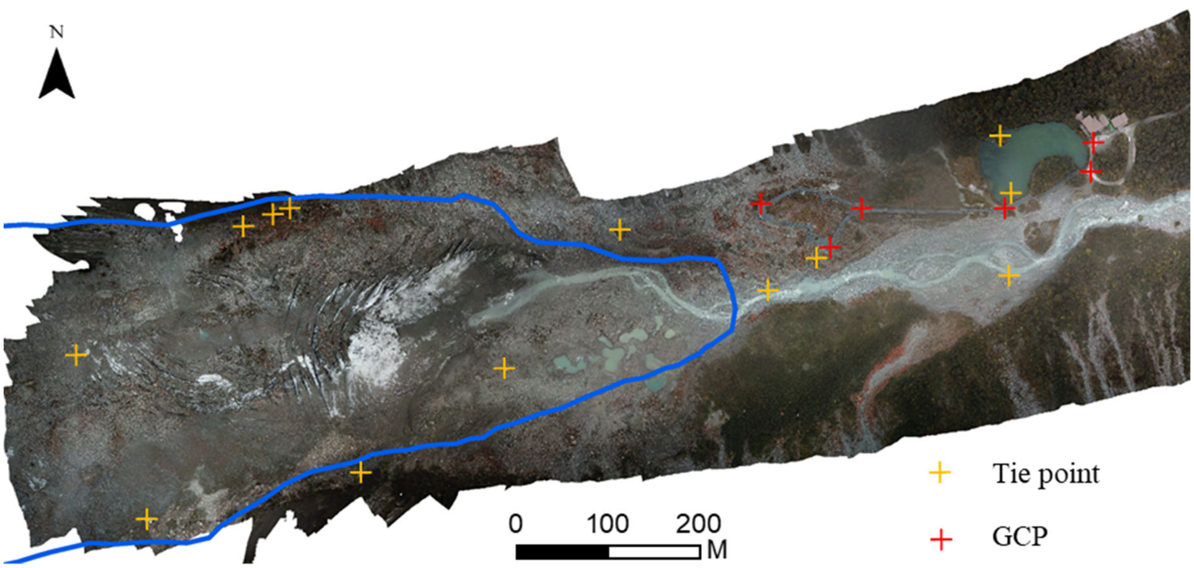

Fig 2. Spatial distribution of the GCPs and the tie points. The background orthophoto mosaic is generated from the dataset of November 5th 2020. The blue polygon indicates the HLG Glacier terminus extent (2009) extracted from the Second Glacier Inventory of China (Liu et al., 2014).

3.2. Method

3.2.1 Image processing

Aerial images were used as input to generate point clouds, Digital Surface Models (DSMs) and orthophoto mosaics by a surface reconstruction workflow in Agisoft Metashape Professional version 1.5.3 (AgiSoft LLC). In addition, some images (Tab. 2 - No.1 and No.2) were extracted by screenshots with a constant time interval from the aerial videos. These extracted images were integrated with the still aerial images to form an input dataset for the 3D surface reconstruction. Agisoft Metashape Professional is now a well-established and widely used 3D reconstruction software in landform investigations (Bash et al., 2018; Rossini et al., 2018b; Rusnák et al., 2018; Verhoeven, 2011).

We followed a standard SfM-MVS processing workflow, as described in many previous studies(e.g., Immerzeel et al., 2014; Rossini et al., 2018b; Ryan et al., 2015; Smith et al., 2016). We used high accuracy settings for image alignment and the embedded GNSS location data for each image to aid georeferencing of the sparse point cloud. The georeferencing was refined using our external GCP locations, and the dense point cloud was then extracted. DSMs and ortho-images were derived from the dense point cloud at the sub-meter resolution, and with centimeter-scale error. We georeferenced the point cloud of November 5th 2020 using our external GCPs, and then registered the remaining clouds to this master cloud using easily identifiable and stable surface features (e.g., giant rocks or erratic boulders) evenly distributed in the glacier snout area. A complete workflow of the 3D scene reconstruction for the case of HLG Glacier is shown in Fig. 3.

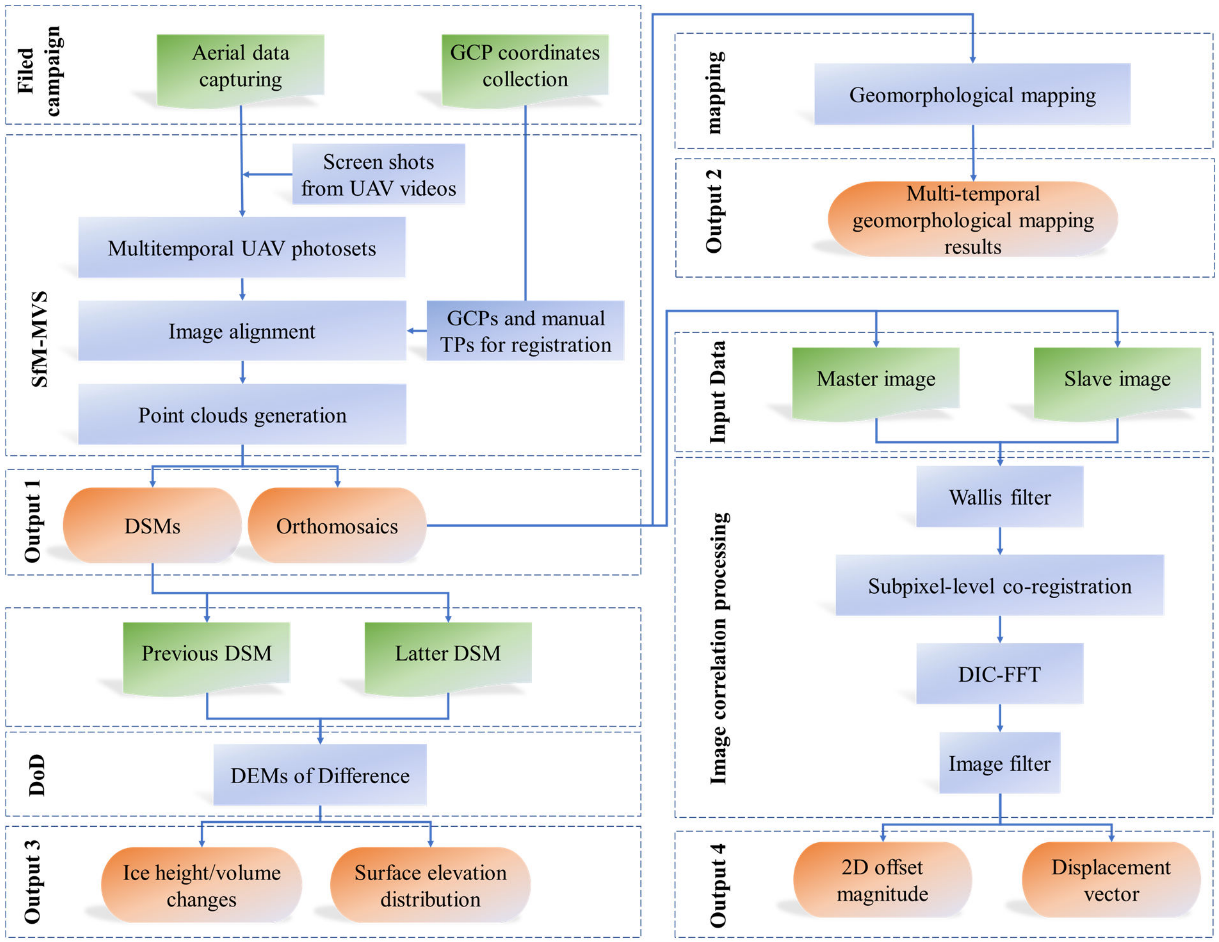

Fig. 3. The workflow of the study, including the generation of DSMs and orthomosaics from SfM workflow (output 1), multi-temporal geomorphological mapping results (output 2), DoD (output 3), and surface displacements from the digital image correlations (output 4).

3.2.2 Geomorphic mapping

The primary datasets for the geomorphic mapping were the orthophoto mosaics (Fig. 3). Their sub-decimeter spatial resolution provided an unprecedented view of the evolving glacier geomorphology, and the opportunity to characterize landform features in exceptional detail (Chandler et al., 2018). The georeferenced orthophoto mosaics were imported to ArcGIS to digitize glacial geomorphic features by visual interpretation, such as glacier terminus extent, calved or collapsed area, ice cliffs, ice crevasses, marginal fresh ice, proglacial river/ponds, periglacial vegetation, supraglacial ponds and lateral landslides. In order to determine the precise identification of the landform features in the HLG Glacier valley, the 3D scene of the point clouds was consulted for cross-checking. For example, the visual assessment of terrain relief from the 3D scene of the dense point cloud was useful for identifying the boundary between the debris-covered glacier and lateral cliff walls.

3.2.3 Comparison between multi-temporal DSMs

Quantifying the surface elevation changes, and their corresponding volume changes is critical for evaluating the landform development. DEMs of Difference (DoDs) represent a possible approach to tracking the landform changes (Wheaton et al., 2009). We used the open-source software Geomorphic Change Detection (James et al., 2012; Wheaton et al., 2009) to compute the ice height changes and the corresponding volumetric variations (Fig. 3). The eight DSMs were re-sampled to 0.5 m/pixel, as a compromise between maximizing information retention and computational efficiency. Seven DoDs were computed from these DSMs, to characterize surface changes between each of the field campaigns. We used Minimum Level of Detection (MinLoD) as a threshold for distinguishing real surface variation from the noise (Fuller et al 2003). A conservative MinLoD of 0.5 m was identified based on the previously published rates of surface elevation change over subsequent ablation seasons.

3.2.4 Surface displacement at the HLG Glacier snout

We also derived glacier flow fields from each pair of orthophotos (resampled to 0.25 m/pixel) because previous work has shown that the surface displacement can be strongly linked with frontal processes – in particular for the glacier frontal ice collapses (Che et al., 2020). The method based on digital image correlation (DIC), also known as feature tracking, is commonly used to identify the movement of common features between subsequent images (Bickel et al., 2018; Heid and Kääb, 2012; Strozzi et al., 2002). Here we used an open-sourced DIC algorithm based on Fast Fourier Transform (hereon, DCI-FFT) (Bickel et al., 2018; Guizar-Sicairos et al., 2008). We employed a Wallis filter to mitigate the negative effect of unsteady lighting conditions in the glacier valley – based on a locally-adaptive contrast enhancement, and filtered the outputs to remove noise and improve the aesthetics of the results (Fig. 3).

4. RESULTS

4.1 Evaluation of the accuracy of UAV-derived data

The accuracy of the DSMs generated by SfM-MVS is predominantly influenced by the quality of the captured images. It is particularly challenging to obtain high-quality images by UAV in the rugged high mountain environment, as the rapidly changing regional weather (e.g., mist or cloud) in the HLG Glacier valley causes different lighting conditions and temporally-variable shadows. Nevertheless, visual assessment of the resulting point clouds, and the very uniform signal of stability in the off-ice areas, suggests that where shadowing was severe and/or variable, those images were not successfully matched (and therefore had minimal impact on the DSMs or orthophotos).

The absolute georeferencing of the DSMs and the orthophotos depends primarily on the quantity and quality of the GCPs and their spatial distribution. We were limited to just six GCPs distributed around the proglacial zone, which somewhat limited the positional accuracy of the products generated from UAV images. However, our strategy of georeferencing only one of these point clouds, and then co-registering the remainder of our data to this 'master' cloud, minimizes the impact of this limitation. Indeed, given that our confidence in the internal (relative) accuracy of the point clouds is high, the resulting DoDs generated between datasets can be considered similarly robust. There may be some minor error associated with the manual placement of tie-points between each pair of clouds, but it is probably negligible given the high number and careful choice of tie-point locations that we used.

Therefore, eight DSMs and orthophoto images were successfully derived from the overlapping UAV imagery (Tab. 2). The number of points in each cloud varied from ~150,000 to ~60,000,000 according to their covered area, and then the point clouds were able to produce DSMs with the spatial resolution no more than 0.36 m/px and orthophotos with a spatial resolution of <0.1 m/px. Georeferencing errors were generally of the order of 0.35 m. All DSMs and orthophotos were resampled to 0.5 m/px and 0.25 m/px respectively for multitemporal DSM comparisons and surface displacement analysis, respectively.

4.2 Geomorphic mapping for tracking glacial feature changes

The overall impression of the tongue of HLG Glacier is shown in Fig 4. The surface of HLG Glacier is covered with a thick debris mantle, below the icefall. Lateral valley relief presents steep cliffs that are the source of debris falling either directly onto the glacier surface, and transported towards the terminus, or buried in the accumulation area beneath snow cover, and carried englacially for meltout in the ablation area (Zhang et al., 2010). Both lateral sides of the HLG Glacier valley are covered with vegetation such as shrubs and trees etc., and several small streams fed by smaller glaciers in the HLG Glacier valley possibly (Figs. 4f and 4g) flow down from higher elevation to link with the supraglacial river networks or subglacial drainage systems as an external supply of the freshwater to the glacier hydrological system. Meltwater runoff and external water supply transfer into the glacier hydrological system by various means such as supraglacial, englacial and subglacial drainage networks. These runoffs combine towards the terminus to form the proglacial river (Fig. 4b).

Clean ice is evident within certain areas of the otherwise thickly debris-covered tongue; one is around the glacier terminus (i.e., Fig. 4c), and the other is around the icefall (Fig. 4i). Around the terminus numerous ice crevasses and ice fractures are evident, especially for the upper part of the frontal collapsed area (Fig. 4d), providing the structural weaknesses that eventually become points of failure in calving events. Large ice crevasses and ice fractures are also evident in the glacier arches (i.e., in the elevation zone ranging from 3850 to 3480 m a.s.l; Fig. 4g) and lower part of the icefall (i.e., around 3900 m a.s.l; Fig. 4i). The presence of these large ice crevasses is somewhat different in size and orientation from those around the glacier terminus, indicating their formation might be related to fast flow through the icefall.

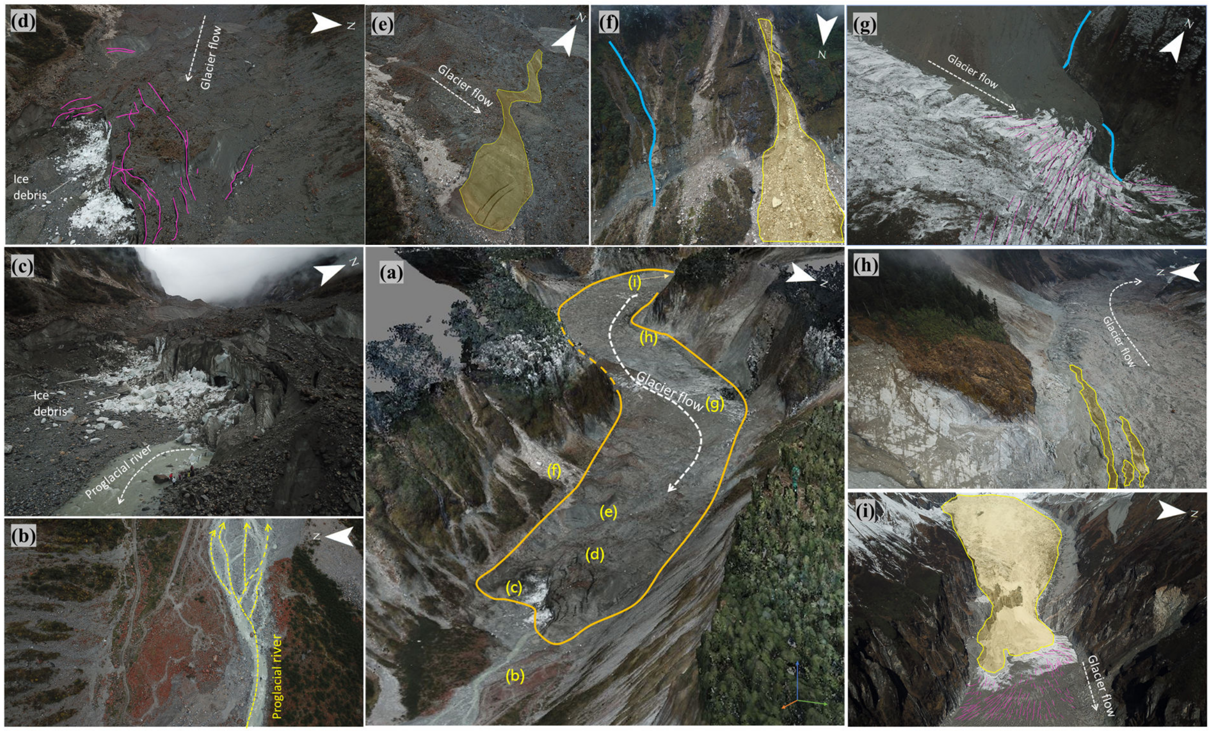

Fig. 4. An example of the three-dimensional representation of HLG glacier with an oblique viewing angle and other photos demonstrating glacial features (dataset of 3rd October 2018). The center image (a) is the oblique view of the dense point cloud of most of the glacier tongue (from the icefall to the periglacial forests) produced by the SfM-MVS workflow. The surrounding images are as follows: (b) shows the proglacial river and periglacial zone; (c) shows the calved ice margin, frontal ice cliffs and the subglacial outlet; (d) shows ice crevasses concentrated around the glacier terminus and calved margin; (e) shows a series of ice cliffs on the glacier surface; (f) shows a lateral landslide in the glacier valley and a seasonal stream; (g) shows an inlet of a lateral stream and ice crevasses centered around the inlet; (h) shows a series of lateral marginal ice cliffs distributed near the glacier arches (3850 to 3480 m a.s.l); (i) shows the lower part of the icefall with an extensive falling and collapsing fresh ice mass.

Over the period of observation, the terminus area of the glacier evolved very rapidly (Fig. 5). In particular, the subglacial channel outlet (i.e., the frontal ice cave) changed its position several times, which subsequently led to multiple variations of the path of the main HLG proglacial rivers. This fluctuation impacted heavily on the glacier terminus position. In order to highlight the effects of collapse events on the glacier retreat, we compared the forward-most (hereon the glacier frontal terminus) and the backward-most (hereon the glacier collapsed terminus) points of the glacier terminus. We generated the centerline of HLG Glacier by using the Open Global Glacier Model (OGGM) (Maussion et al., 2019), and used this to define these positions. The area not affected by the subglacial channel (and therefore collapse/calving processes) retreated approximately 132.1 m from 2017 to 2020 (i.e., the distance highlighted by yellow dash lines in

Fig. 5), in contrast to the area to the more dynamic south side of the glacier, which retreated by more than 236.4 m over the same period (i.e., highlighted by blue dash lines in Fig. 5). The fastest recession for the terminus of HLG Glacier affected (glacier collapsed terminus) or non-affected (i.e., glacier frontal terminus) by the ice collapsing events occurred between 2018-10-28 and 2019-10-03. It is notable that both glacier margins (i.e., glacier frontal terminus and glacier collapsed terminus) have suffered substantial terminus retreating due to ice collapsing events over a relatively short time span as shown in Fig. 6c.

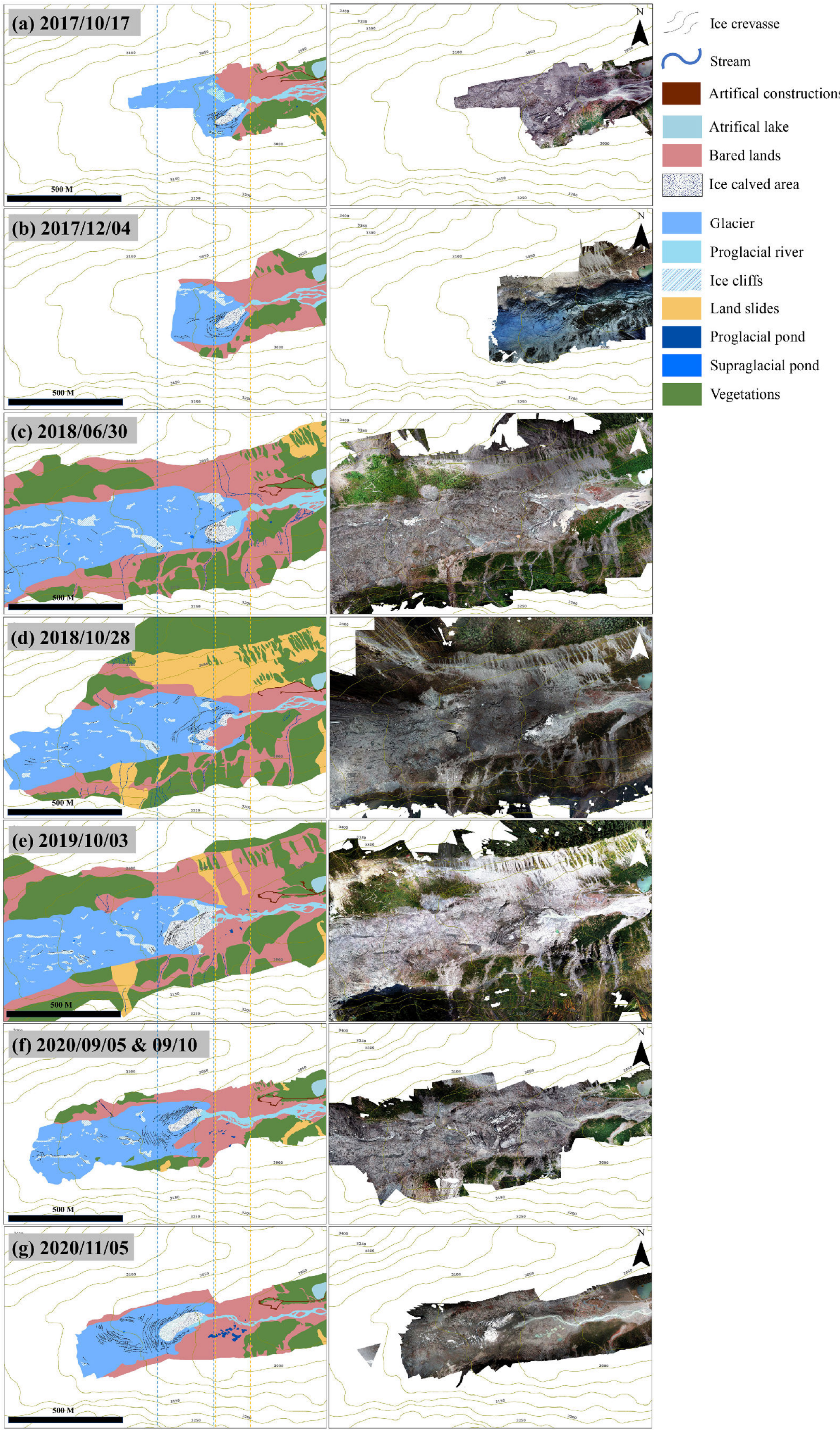

(a) 2017/10/17
(b) 2017/12/04
(c) 2018/06/30
(d) 2018/10/28
(e) 2019/10/03
(f) 2020/09/05 & 09/10
(g) 2020/11/05
500 M
N
Ice crevasse
Stream
Artifical constructions
Atrifical lake
Bared lands
Ice calved area
Glacier
Proglacial river
Ice cliffs
Land slides
Proglacial pond
Supraglacial pond
Vegetations

Fig 5. Results of geomorphic mapping based on the orthophoto mosaic. Top to bottom (a to g) indicated the glacier terminus changes and the changes of surrounding glacial landscapes from October 2017 to November 2020. Left column and right column are the mapped illustration and orthophoto mosaic, respectively. We used one figure to show 2020/09/05 and 2020/09/10 as their interval is too short to identify geomorphic changes. Although the area mapped in the seven maps are different, they provide sufficient coverage of the glacier terminus to show the evolution surrounding it. The blue and yellow dash lines represented extreme changes of the glacier collapsed terminus and glacier frontal terminus between 2017/10/17 to 2020/11/05, respectively.

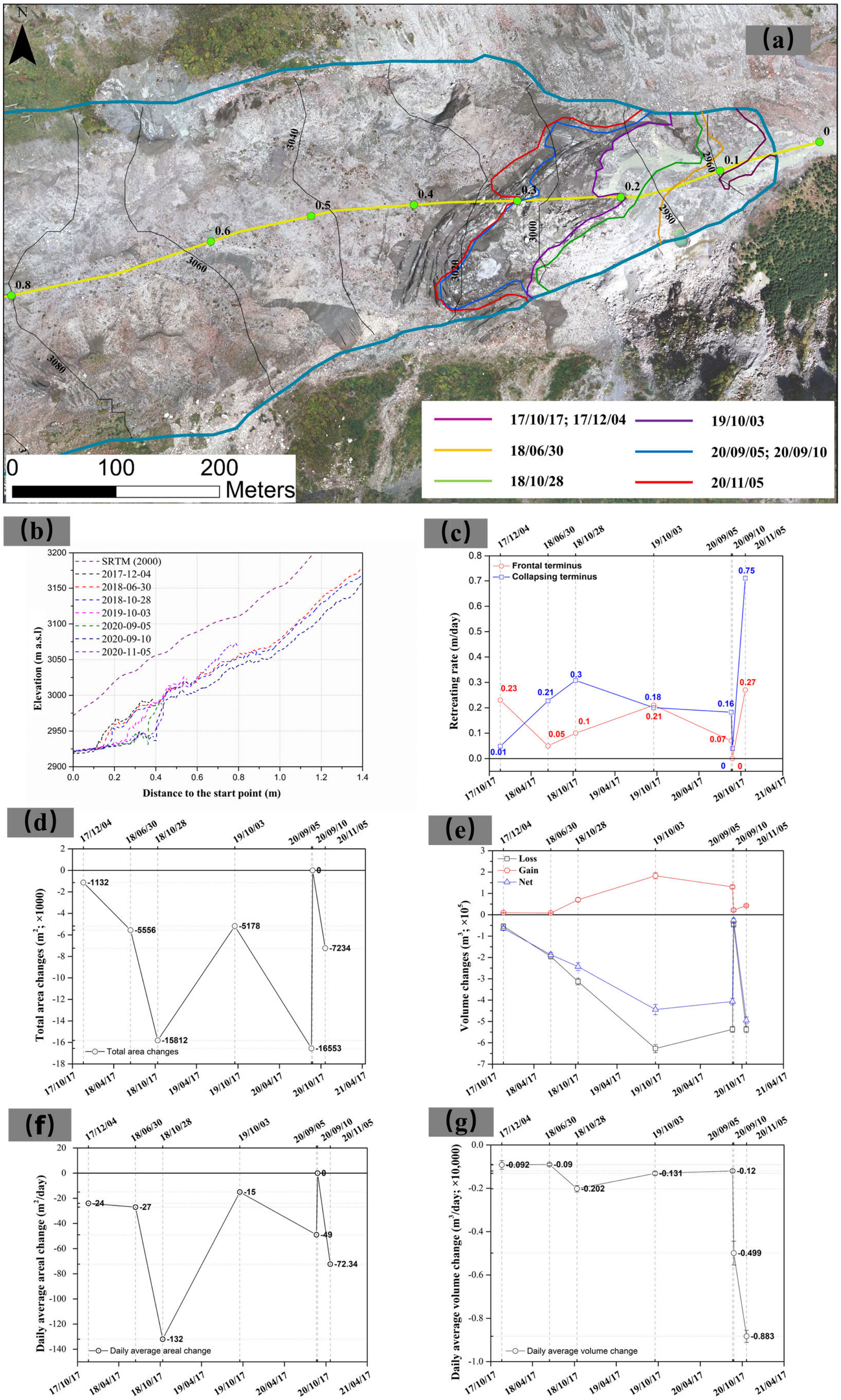

(a)
N
0
0.1
0.2
0.3
0.4
0.5
0.6
0.8
2960
2980
3000
3020
3040
3060
3080
17/10/17; 17/12/04
19/10/03
18/06/30
20/09/05; 20/09/10
18/10/28
20/11/05
0 100 200
Meters
(b)
SRTM (2000)
2017-12-04
2018-06-30
2018-10-28
2019-10-03
2020-09-05
2020-09-10
2020-11-05
Elevation (m a.s.l)
Distance to the start point (m)
(c)
Frontal terminus
Collapsing terminus
Retreating rate (m/day)
(d)
Total area changes
Total area changes (m², ×1000)
(e)
Loss
Gain
Net
Volume changes (m³; ×10⁵)
(f)
Daily average areal change
Daily average areal change (m²/day)
(g)
Daily average volume change
Daily average volume change (m³/day; ×10,000)
17/12/04
18/06/30
18/10/28
19/10/03
20/09/05
20/09/10
20/11/05
17/10/17
18/04/17
18/10/17
19/04/17
19/10/17
20/04/17
20/10/17
21/04/17

Fig 6. Longitude profiles for the HLG Glacier terminus (a and b) and statistical analysis about the HLG Glacier terminus evolution (c-e). (a) shows the spatial distribution of the center flowline of the HLG Glacier and terminus line of HLG Glacier from 2017-10-17 to 2020-11-05. The HLG Glacier extent (2009) was extracted from the Second Glacier Inventory of China and the background orthophoto mosaic is from the 2019-10-03 dataset. (b) shows the profile along the center flowline of HLG Glacier. Profile of SRTM is listed as additional information for reference. (c) shows the retreat distances for the glacier frontal terminus and glacier collapsed terminus. (d) shows the terminal area changes due to the glacier retreat. (e) volumetric changes due to glacier terminus evolutions. (f) daily average areal changes. (g) daily average volume changes.

Tab. 3 shows the quantitative analysis of the variation of the HLG glacier terminus. The total areal ice loss between the first and last field campaigns was 51,465 m^2. The fastest reduction in area was during the campaign of June 30th 2018 to October 28th 2018 (i.e., 120 days intervals; 15,812 m^2) and the campaign of October 3rd 2019 to September 5th 2020 (i.e., roughly annual intervals; 16,553 m^2). The recession was evidently highest during the glacier ablation seasons and has generally been increasing in rate through time. The capture of two frontal ice collapsing events, one of which was substantial, confirms the importance of the frontal ice collapsing event as an ablation mechanism for this glacier (i.e., Tab. 3g). This ice collapsing event caused approximately 7,234 m^2 in areal recession over a short interval.

Comparing the surface profiles extracted from UAV-derived datasets with the profile extracted from SRTM (2000) reveals that snout of HLG Glacier underwent an overall lowering of approximately 50 m over the nearly two-decade period. The area within 400 m of the terminus is the main zone for terminus retreat and ice collapsing (Fig. 6a). As revealed by the surface profiles in Fig. 6b, terminus retreated successively with varying degrees of lowering. However, in the lower part, approximately 350 m along the center flowline, three surface profiles for 2020-09-05, 2020-09-10 and 2020-11-05 are particular notable. This pattern might be induced by the rapid propagation of ice crevasses from the glacier collapsed terminus towards the upper part of the glacier snout. With the enhanced water-glacier interactions beneath the glacier bodies or above the englacial/subglacial channels, it is feasible that the deep crevassing may be intensified due to the thermal erosion, producing an unexpected ice surface lowering or the roof lowering of subglacial/englacial channels even for some distance from the terminus area. The primary cause for this event is probably the basal melting and positive feedbacks associated with the collapse events, and the impact on strain rates which will have weakened the surrounding ice and along the subglacial channel and outlet.

The near-vertical lines occurring between 2020-09-05 to 2020-11-05 are clear visible in Fig. 6c, d and e, and they indicate the impact that ice collapse events can have on glacier recession rates. Although the ice collapsing events have a moderate effect on the daily average areal reduction (i.e., Fig. 6f), its influence on the daily average ice volume changes is obvious (i.e., Fig. 6g).

4.3 Surface elevation and volumetric changes

Multi-temporal DSMs were differenced to quantitatively measure the changes of HLG Glacier during the period of observation (Fig. 7). The greatest surface elevation changes (of roughly -40 m over a 56-day period) occurred in the lattermost pair of DSMs, which included a confirmed large ice calving event. Several other periods showed surface lowering in excess of 30 m, which we also interpret to portray collapse or calving events. As the ice thickness is known to range between 30 to 40 m around the terminus area of the glacier, it indicates either calving can propagate all the way to the glacier bed, or in the case of collapse events, that the subglacial chamber formed by the outlet channel is large.

More broadly, the terminus of HLG Glacier presented dramatic surface lowering and ice mass loss during 2017 to 2020, with an overall ice loss volume of $184.61 \pm 10.32 \times 10^4$ m^3. The detailed ice volume changes and the histogram of the surface elevation change is shown in Fig. 7. The statistics are summarized in Tab.3. Tab. 3d and 3e present similar interannual magnitudes of total ice volume changes, that is - $44.41 \pm 2.41 \times 10^4$ m^3 and - 40.74 ± 1.62 × 104 m3. However, the total ice volume changes over the lattermost period have the maximum volumetric loss (- 49.51 ± 1.58 × 104 m3) revealing that a single calving event can exceed the interannual ablation from non-mechanical processes. We note here though that our DoDs cannot account for any ice emergence, meaning that ablation may be underestimated.

From the aspect of the daily average of ice volume loss, ice loss due to the small ice collapsing event (i.e., Tab. 3f) is - $0.50 \pm 0.16 \times 10^4$ m^3, roughly four times the daily losses recorded in the interannual pairs (i.e., Tab. 3d and 3e). Ice volume lost during the large ice collapsing event (Tab. 3g) was about 1.7 times that of the small ice collapsing event (Tab. 3f).

Table. 3 The statistical analysis of the HLG Glacier terminus changes

No.	Model pair (y/m/d)	Intervals (days)	Frontal/collapsed terminus retreats (m)	Total area changes m^2 ($\times10^2$)	Average areal change m^2/day	Ice height changes (max/min/mean)	Total volume change m^3 ($\times10^4$)	Average volume change m^3/day ($\times10^4$)	Seasons
a	17/10/17-17/12/04	48	1.1/0.3	- 11.32	- 24	5.10/- 11.36/- 1.10	- 4.42 ± 0.98	- 0.09 ± 0.02	End of the ablation season
b	17/12/04-18/06/30	208	10.3/44.5	- 55.56	- 27	4.86/- 16.84/- 2.57	- 18.71 ± 1.13	- 0.09 ± 0.01	Roughly whole accumulatio n season
c	18/06/30-18/10/28	120	11.8/36.4	-158.12	- 132	9.08/- 31.20/- 2.01	- 24.30 ± 1.82	- 0.20 ± 0.02	Major ablation season
d	18/10/28-19/10/03	340	71.6/60.3	- 51.78	- 15	12.81/- 38.31/-2.36	- 44.41 ± 2.41	- 0.13 ± 0.01	Annual
e	19/10/03-20/09/05	338	22.1/52.8	- 165.53	- 49	13.60/- 35.88/-4.01	- 40.74 ± 1.62	- 0.12 ± 0.01	Annual
f (MA-s)	20/09/05-20/09/10	5	15.2/42.1	≈ 0	≈ 0	8.82/- 30.34/- 0.33	- 2.52 ± 0.78	- 0.50 ± 0.16	Several days in ablation season
g (MA-l)	20/09/10-20/11/05	56		- 72.34	- 129	9.47/- 41.83/- 5.32	- 49.51 ± 1.58	- 0.88 ± 0.03	Major ablation season
Total	17/10/17-20/11/05	1115	132.1/236.4	- 514.65	- 46.16		~ 184.61 ± 10.32	~ 0.17 ± 0.01	

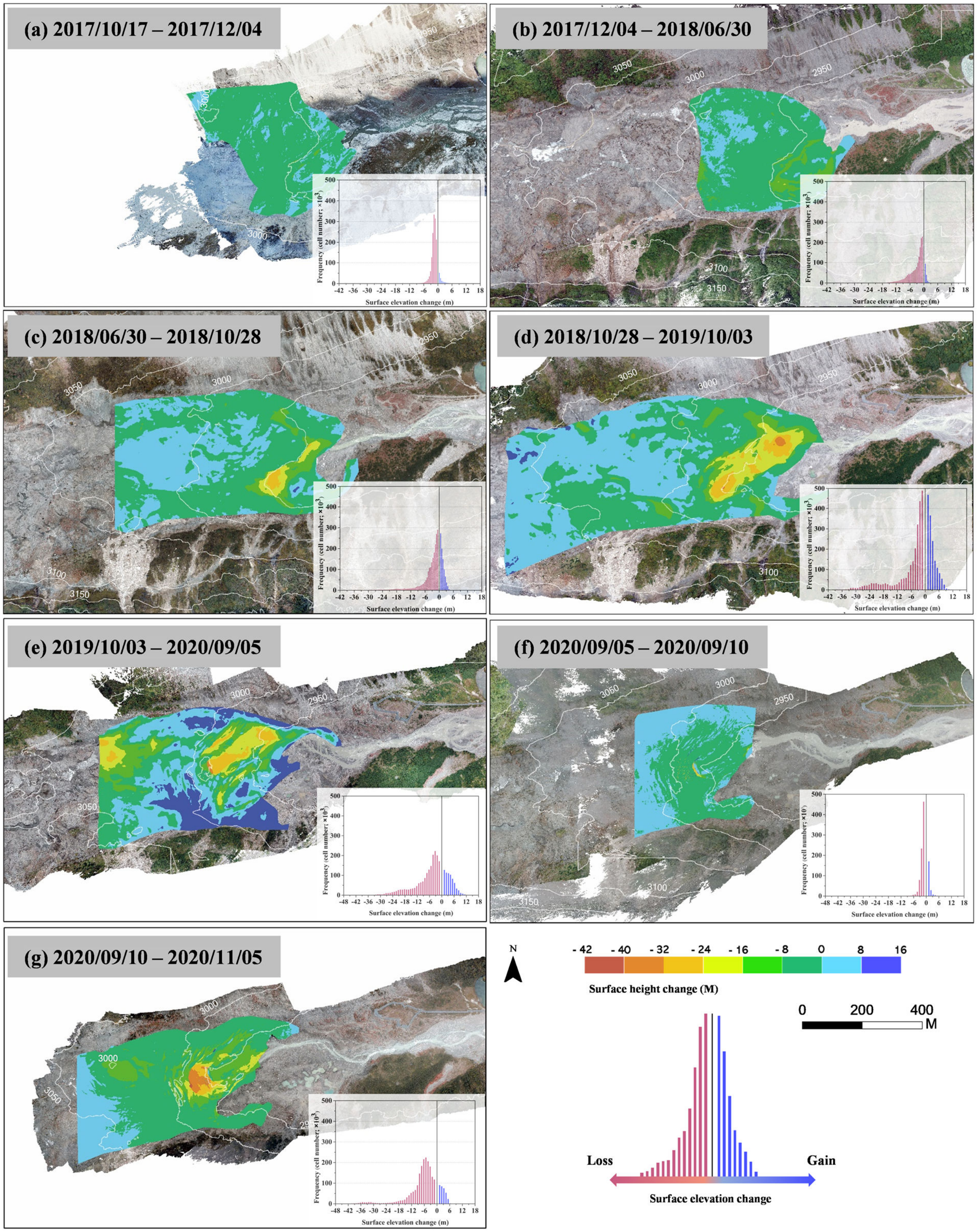

Fig 7. Ice height changes and the distribution of glacier surface elevation changes from October 2017 to November 2020 (a to g). The background image is the latter orthophoto image from each pair and the contour line is derived from the DSM of the latter for each DoD. The insert histograms show the surface

elevation changes for each compared pair.

4.4 Spatial distribution and magnitude of surface displacement at the glacier snout

As the area of datasets of 2017-10-17 and 2017-12-04 were too small to produce valid surface displacement, we used the five datasets from 2018-06-30 to 2020-11-05 to generate four surface displacement maps for the HLG Glacier snout. Since the area for image correlations for each pair was variable, we used different window sizes for the offset tracking (Tab.4).

Table. 4 Window sizes for each pair

Date	Window size for DIC-FFT (pixels)
2018-06-30 to 2018-10-28	80
2018-10-28 to 2019-10-03	90
2019-10-03 to 2020-09-05	100
2020-09-05 to 2020-11-05	60

The 2D offset magnitude and displacement vectors for each pair illustrate the spatial distribution of the surface velocity for the glacier snout (Fig. 8). These four 2D offset magnitude maps reveal that the area with high offsets (i.e., dark red) are mainly distributed around the location of ice crevasses (e.g., Figs. 8a and c) or ice cliffs (e.g., Fig. 8b) with the maximum magnitude of about 10 m. Dashed polygons in Fig. 8 (i.e., yellow in the left column, and black in middle and right column) were used to indicate the areas in front of the glacier collapsed front. Relatively high surface offset magnitude was found around northern and western edges of theses polygons, which may be caused by crevassing and the developing of ice cliffs. There is a clear distinction in the flow dynamics between the area affected by calving and collapse and the area not affected by mechanical processes. There is a clear signal of flow being dominantly towards the collapsing region (right column in Fig. 8), i.e., most of arrows point to the northwest and west side of these polygons (e.g., Fig. 8a and b), which also shows how ice collapsing events develop spatially. In other words, in the displacement vector maps, areas with consistent directions and densely distributed arrows pointing to the end of the glacier are often potential areas where ice collapsing events can occur. There is clear distinction between the displacement vectors in in Fig. 8 a and b versus those in Fig. 8c and d; those in Fig. 8c and d do not closely concentrate on the northwest and east side of the polygons (i.e., the frontal collapsed margin), with some vectors even presenting the nearly ring-shaped pattern indicative of surface lowering caused by the roof collapsing of subglacial channel (Fig. 8d).

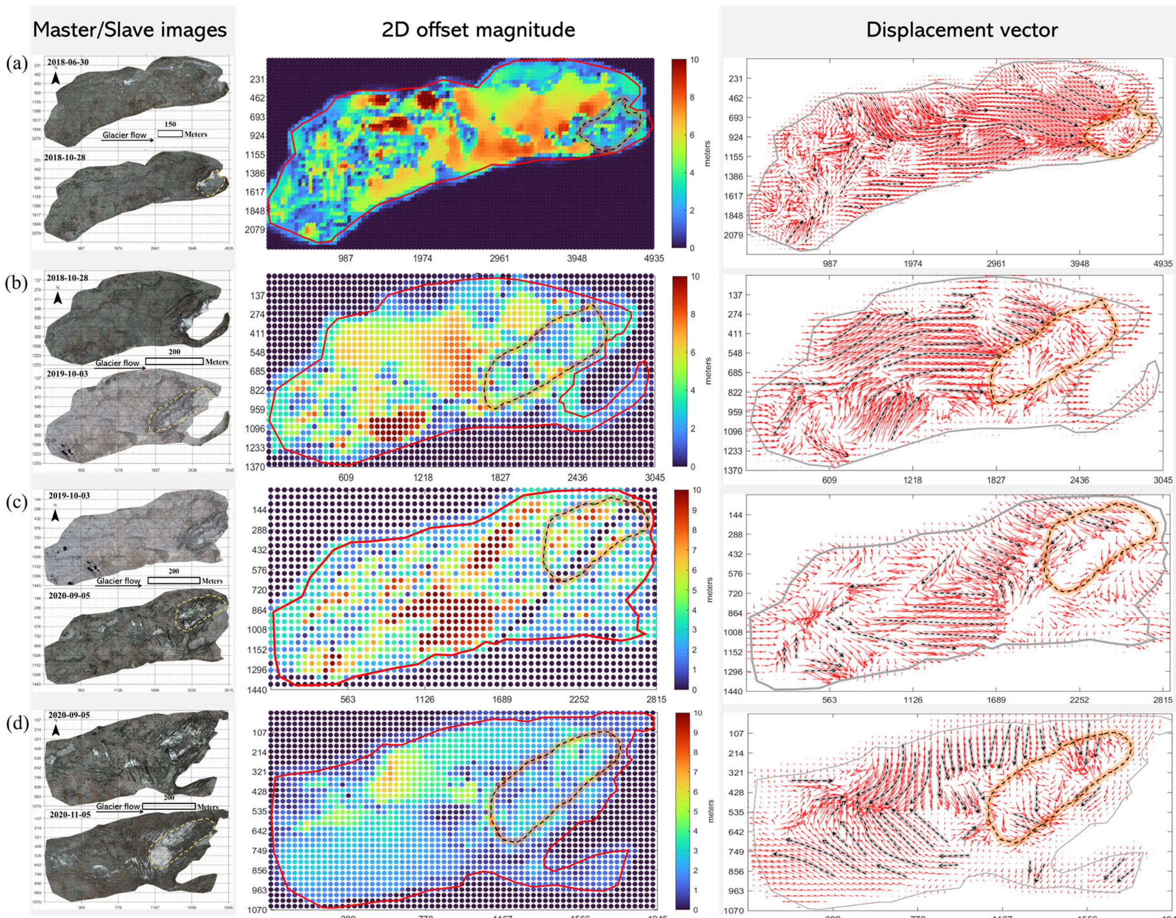

Fig 8. An illustration for the surface displacement of HLG Glacier generated by the method of DIC-FFT during the period from 2018-06-30 to 2020-11-05. The left, middle and right column show the image pair (i.e., up: master image; down: slave image), 2D offset magnitude maps and Displacement vectors, respectively. Yellow dashed polygons in the left column represent areas in front of the glacier collapsed front, and the black dashed polygons in the middle and right columns also represent the same area.

5. DISCUSSION

5.1 The significance of mechanical ablation to ice loss

The measurements of daily area change revealed that the frontal ice collapsing events of the glacier snout may not affect the glacier area immediately, but may exert lag and significant impacts on the areal shrinkage. For example, the area changes caused by an ice collapsing event (i.e., 2020/09/10 - 2020/11/05) account for more than 14% (i.e., 7234 m^2) of the total area changes (i.e., 51465 m^2) for the studied area. Owing to the isolated chunks of ice that might be melted and transferred by the glacier river easily, these effects were mainly induced by the ablation of massive dead ice stripped off from the glacier snout due to the ice collapsing events and enhanced subsequent melting of the exposed fresh ice. As for the ice volume changes, the total volumetric change for the observed area in the HLG Glacier snout was about 184.61 ± 10.32 $\times 10^4$ m^3 from 2017 to 2020. Based on the intercomparisons of ice volume changes for each pair, it is found that a large ice collapsing event in the glacier snout can contribute huge ice mass losses in a short time, which could exceed the previous interannual ice volume changes. The daily volume changes obtained for the relatively longer observation periods range between 0.09 to 0.20 $\times 10^4$ m^3. However, we observed that a single ice collapse events can routinely remove ice volumes of 0.50± 0.16 to 0.88 ± 0.03 $\times 10^4$ m^3 per day. These statistics about ice volume changes indicate the dominant impact of ice collapse as an ablation process, especially over the summer season. Consequently, and similar to lake-terminating glaciers (e.g., Carrivick and Tweed, 2013), its retreat may be controlled by the interactions of water and glacier near the glacier terminus. Furthermore, projections of the recession rate of the HLG Glacier that rely solely on surface mass balance probably underestimate its evolution, since the frontal ice collapsing might be more frequent and larger under the context of warming. Continuously collapsing events that occurr at the glacier terminus may causes an enhanced hydrological responds, leading to high magnitude debris flow or river blockage, as well as other glacial-hazards in this region (Liu et al., 2018; Lu and Gao, 1992)

5.2 Mechanical ablation pattern of HLG Glacier snout

Our multi-temporal UAV imagery shows very clearly that the major ice collapse events occur around the position of the outlet of the subglacial channel. In common with marine- and lacustrine-terminating glaciers, ice crevasse patterns near to the frontal margin appear to determine the size and frequency of subsequent calving events. Areas of ice loss detected in 2019 tie in almost perfectly with the presence of deep crevassing in the imagery acquired in 2018, for example, and similar patterns can be identified between September 2020 and November 2020 datasets. Our geomorphological mapping shows very clearly the evolution of these features through time, with crevasse traces likely emerging from the icefall and being advected down-glacier beneath the surface debris, before being re-opened as lines of weakness by the change in stress around the terminus area. Although it is not possible to gauge crevasse depths from our data, the DoDs suggest that either these failures are able to propagate through the full ice thickness to the bed, or the subglacial channel associated with the outlet portal is large enough to induce a collapse event. Either way, the ice that is subsequently deposited in the outlet channel is quickly removed by meltwater, making this a highly efficient mechanism of ice ablation. Another study about the drainage system of the HLG Glacier indicated that the subglacial drainage network is a longitudinal-oriented steady system, which is also confirmed by the frequent collapsing subglacial conduit outlets (i.e., ice fracturing due to the expansion of the subglacial channels), where the hydraulic efficiency is high (Liu et al., 2018).

As discussed in Section 4.2, in the lower part of the center flowline (Fig. 7b), a similar abnormal decline occurred at three surface profiles (i.e., 2020-09-05, 2020-09-10, and 2020-11-05). This decline may also correspond to the surface lowering or the roof collapsing of subglacial conduits (Fig. 9a), even for the upper section of the glacier terminus (Fig. 9f).

Additionally, ice height changes and their distributions also suggested that the large magnitude of an ice collapse event can facilitate the full-thickness ice fractures to remove massive ice chunks and accelerate the glacier retreating. Analysis of the spatial distribution of the ice crevasses and the collapsed zone between successive maps reveals that areas with dense ice crevasses were more likely to develop as areas of ice collapse in the future. This can clearly be seen between Fig. 8c and 8d, with the area of fast flow in Fig. 8c (near 1689 along the x-axis) becoming the collapsed front in Fig.8d. For the case in Fig. 9d, these fast flow arrows are not even concentrated at the glacier collapsed terminus, but form a ring-shaped pattern (or a cluster of arrows from northeast and southeast) at the upper section of the glacier terminus, which implies the destabilization and collapse of the roof of the subglacial/englacial channels (Egli et al., 2021). By comparing the image of 2021-07-28 and 2021-09-02 (see Fig. 9e and f), this potential collapsing location is fully validated. It is possible given its timing that seasonally-enhanced precipitation and meltwater influx into the glacier led to increasing pressure on the hydrological system within the glacier, exceeding its capacity and resulting in mechanical instabilities (Mair et al., 2003). This ablation pattern seems a common feature for valley glaciers as evident by previous studies (e.g., Kavanaugh and Clarke, 2001; Mair et al., 2001, 2002a, 2002b), which is probably linked to the reorganization of the subglacial drainage system and significant ice motions on the glacier surface. Based on this interpretation, the potential trigger for this pattern is induced by the reduction of basal drag and the resultant increase in basal motion. Thus, for this reason, either the events are facilitating crevassing for the frontal ice and ice motions, or the subglacial drainage provides additional lubrication, hence enhancing the ice flow.

5.3 Control of mechanical ablation

5.3.1 Proglacial waterbodies

The persistence of proglacial waterbodies partly exacerbates the instability of the glacier frontal margin and facilitates the glacier retreat to some extent (King et al., 2019; Liu et al., 2020). Although the HLG Glacier is a non-lacustrine glacier (i.e., no proglacial lake), HLG Glacier has a well-developed drainage network connecting the supraglacial, englacial, and subglacial spaces (Liu and Liu, 2012; Liu et al., 2018). Melt streams from other small hanging or valley glaciers distributed in the HLG basin flow into the HLG Glacier via the drainage network (Liu et al., 2018). This drainage network can discharge runoff (including both melting water and overland flow from off-glacier) through the outlet in the glacier terminus, which has formed a shallow pool beneath the glacier terminus and these pools have been observed after collapsing of the ice above (Fig. 9c and d). These pools, which are fed by the drainage system of the glacier, play a similar role in water-glacier interactions compared with lake-terminating glaciers as it has been observed as stagnant water bodies. It is difficult to know how far these subglacial pools extend up-glacier, but it is likely that they at least facilitate an environment where the ice and water mutually interact continuously, which may weaken the stable structure of the glacier sole, even to form weakness lines for further potential ice fracturing.

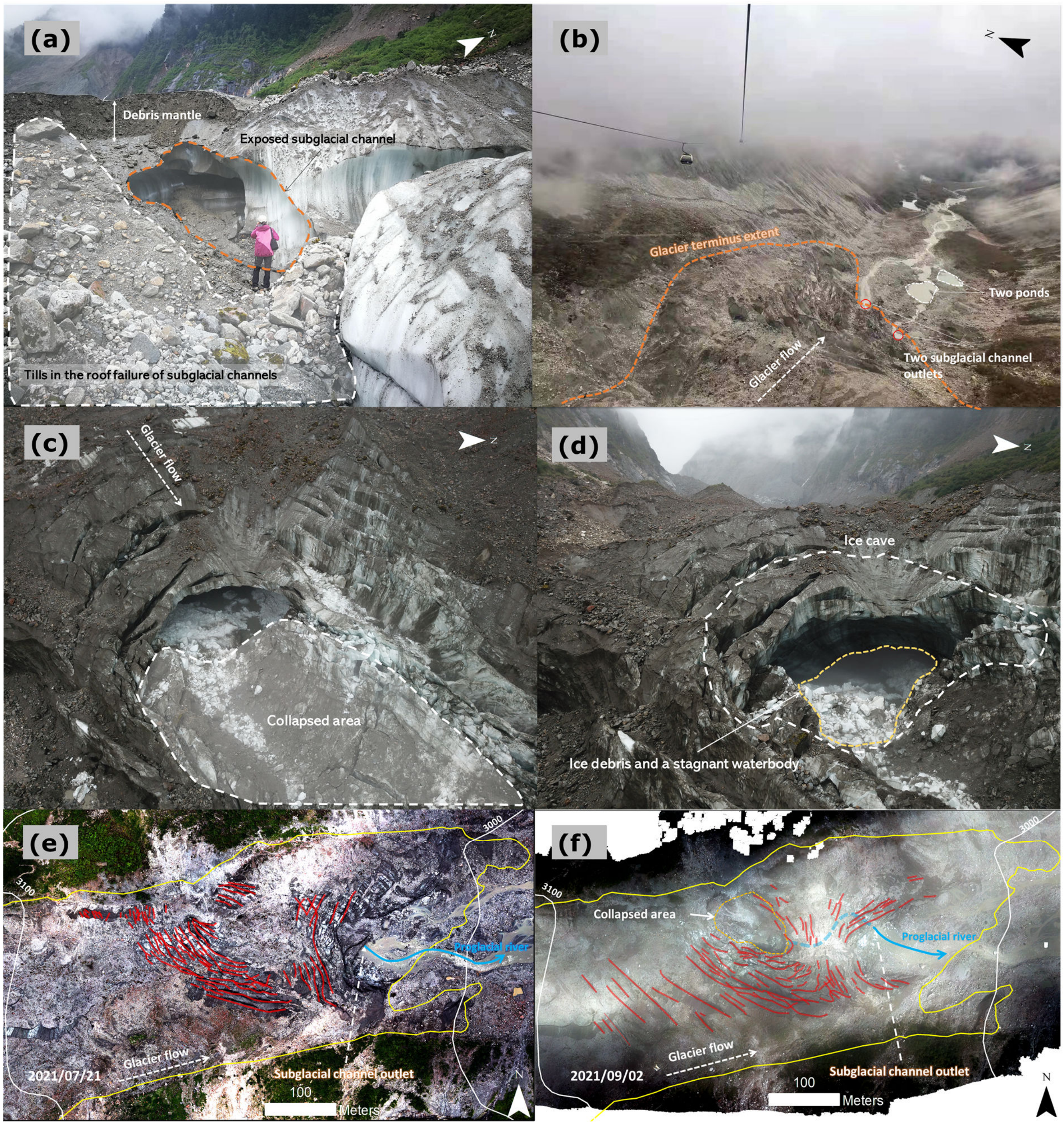

498 Fig 9. (a) The roof collapsing/failure of a subglacial channel in the upper part of the HLG Glacier terminus and the cavity of the subglacial channel was exposed due to the roof collapsing (Date of the photo taken 2018-06-23); (b) A observation of HLG Glacier snout from photographing in cable car by locals (2021-04-28). Two subglacial outlets were found and two ponds were connected and fed by a newly emerged proglacial river channel; (c) and (d) show the landscape of the glacier terminus on 2020-09-10. A collapsed area is located at the front of the glacier terminus (i.e., ice cave) and it blocked the runoff flow from the subglacial outlet and formed a stagnant water body beneath the glacier terminus; (e) and (f) were the ortho-mosaics of 2021-07-21 and 2021-09-02, and red polylines indicate the ice crevasses. The yellow dashed polygon in (f) shows the collapsed area and light blue dashed line indicates the potential subglacial channel.

During the major ablation season (i.e., May to October; also, the rainy season) of the HLG Glacier, the seasonally enhanced glacier runoff likely feeds more water into these pools, subsequently impacting the frequency of ice collapse events. The collapsed terminus of the HLG Glacier is roughly cave-shaped with an arch-shaped ice roof, which is often filled by ice debris (Fig. 9c and d). Collapsing occurs when ice crevasses continue to crack down through the arch-shaped ice roof and simultaneously the grounded ice sole becomes unstable due to water-glacier interaction. This leads to the exposure and deepening of further fractures as a consequence of the tensile stresses. Periodically, massive ice deposits can bury the outlet of the subglacial river, forcing the river to find another path and develop a new outlet and cave, and starting another cycle of undercutting, collapse, and fracture exposure. Previous studies on the drainage system of the lower part of the HLG Glacier tongue indicate that some small supraglacial lakes existing from April to May with a short life cycle may be drained completely by fully-connected englacial and subglacial conduits, thereby facilitating the mechanical ablation (Liu and Liu, 2012; Liu et al., 2018). Our mapping results also indicated the existence of supraglacial ponds between the elevation of 3000 to 3100 m a.s.l. (Fig. 6)

The HLG Glacier, which is representative of many other land-terminating glaciers in SE TP, has intensive water-glacier interactions at the frontal ice margin (i.e., the outlet of the subglacial channels), which is evidently responsible for the ice collapse/calving events similar to lake-terminating glaciers. Although there is no proglacial lake at the HLG Glacier termini, several small ponds have formed in the periglacial land around October 2019, and have expanded to a string of connected ponds around November 2020. Furthermore, recent observations of the HLG Glacier snout by locals in April 2021 showed that these connected ponds continue to expand (Fig. 9b). The pond closest to the glacier is fed by a new stream emanating from the glacier terminus, despite the adjacent main glacier river remaining in a similar geomorphic pattern as before. These recent field observations combined with the previous UAV images suggest that a proglacial lake might to be formed at the glacier terminus. Further, with the initiation and the development of the proglacial lake, the frontal ice-marginal collapse events could well be enhanced due to intensified water-glacier interactions (e.g., subaqueous melting or buoyancy-derived weak waterline), furthering forming a similar circumstance to the ice-marginal lake and facilitating the glacier receding.

5.3.2 Subglacial channel networks

HLG Glacier has a longitudinally steady subglacial channel network in the lower ablation region with a relatively high hydraulic efficiency (Liu et al., 2018). The subglacial drainage system of temperate glaciers transforms into a fast drainage system around the beginning of the ablation season and continues the high drainage capacity until the end of the ablation season (Fountain and Walder, 1998; Hooke, 1989; Liu and Liu, 2010; Walder, 2010). As for HLG Glacier, within the period from May to November, nearly all water from rain and melting enters the glacier via the crevasses and flows within the seasonal efficient drainage networks. In this situation, large amounts of water will flow through the englacial and subglacial drainage networks until it drains into the proglacial rivers (Liu and Liu, 2010). The increase in water volume and water pressure in the subglacial drainage system may result in intensified ice-water interactions, leading to more intense ablation. Under the constant impulse of such ablation, the slightly crevassed glacier terminus tends to be more triggered to produce ice collapsing events, even for the non-frontal terminus area (Fig. 9a). with the combined efforts of crevassing and thermal erosion within the subglacial drainage system, roof failures of subglacial channels can be clearly observed (Fig 9e and f). Once the cavity has formed, it is easier to ablate due to the exposure to air, thus leading to more collapsing events (Egli et al., 2021)

With the thinning of the glacier ablation zone, ice creep may not compensate for the expansion of drainage channel walls due to the intensive ablation. The destabilizations of stress-strain balance in ice bodies were exacerbated due to the intensive englacial and subglacial ablations, thereby ice fracture (e.g. ice crevasses and ice collapse), and thus forming terminus ice cliffs (Mei et al., 2013; Nye, 1951; Thorsteinsson et al., 2003). Additionally, the dramatic retreating of the HLG Glacier over years may have forced the glacier terminus to retreat into a rugged and complex basal terrain, which is unsuitable for the thinned glacier terminus to maintain the stress balance, thus facilitating the ice fracturing. Successive observations have shown that the icefall, the link between the upstream firn basin and the downstream glacier tongue, is gradually becoming thinner and narrower. This situation suggests that the supply of mass from upstream is declining, which is probably one of the factors leading to the rapid thinning of the downstream glacier and thereby to stress destabilization and ice collapse.

5.4 Potential effects of decoupling from climate change

Lake-terminating glaciers have been influenced by the presence and behavior of ice-marginal water bodies, such as ice-marginal morphology, physical stability, and glacier dynamics (Carrivick and Tweed, 2013b). A proglacial lake augments the ice mass loss and glacier velocity as the warm water transfers heat to glacier bodies and forms thermally induced melting and then controls the calving by undercutting. In this base, the glacier might be partly decoupled with the climate change under the impact of the ice-marginal lake (Carrivick and Tweed, 2013b; Kirkbride, 1993; Kirkbride and Warren, 1999). For HLG Glacier, the glacier snout is also slightly immersed in its proglacial waterbodies and experiences high pressure in the seasonally efficient drainage networks (Liu and Liu, 2010), which forms a water-rich environment similar to the case of a lake-terminating glacier. Firstly, a stagnant pond beneath the glacier terminus was observed due to the exposure of the cavity of the frontal ice cave (Fig. 9c and d), and considerable water was discharged by the seasonal varied proglacial river even in the winter (Fig. 5) (Liu et al., 2018). These water bodies (i.e., pond beneath the glacier terminus and proglacial river) may continually weaken the structure of glacier base as discussed in Section 5.3.1.

The subglacial channel of the lower part of the ablation zone was examined as a stable and highly efficient drainage system during the whole ablation season. This subglacial drainage system needs to handle considerable runoff from streams of external tributary, precipitation, and the melting runoff of the glacier itself as discussed in the Section 5.3.2. Therefore, the local ice flow and magnitude of the subglacial ablation might be strongly impacted due to the long-standing but seasonal enhanced subglacial drainage system, inducing ice collapsing in some cases (Fig. 9a, c, and d) (Liu et al., 2018). Furthermore, some supraglacial ponds with a short life span were found between the elevation of 3000 to 3100 m a.s.l. (Fig. 5). These supraglacial ponds may be delivered to either internal conduits or ponded crevasses by supraglacial drainage networks, then being discharged completely by fully-connected englacial and subglacial channels (Liu and Liu, 2012; Liu et al., 2018). Thus, there are extensive interactions between glacier and water in HLG that occur in the proglacial river, subglacial environment, and even in the supraglacial and englacial drainage system. In this scenario, heat can be transferred through mainly three ways in the terminus of HLG Glacier: a highly dynamic proglacial river and shallow pond beneath the glacier snout keeping the glacier snout in a state of continuous water-glacier interactions; a well-developed subglacial channel network and seasonally enhanced volume in conduits also allowing interactions of heat subglacially and englacially; and heat may be delivered by ponded water in the crevasses supplied from external precipitation or glacier surface runoff. Therefore, it is analogous that the mechanical ablation that occurred around the terminus of land-terminating by ice collapsing and frontal ice calving can be seen as an amplifier in its process of ice mass loss, which exacerbates the glacier retreating. To some extent, when the intensity of mechanical ablation is strong, it may have been possible to approximate the effect of the proglacial lake.

It is inarguable that the glacier-climate dynamics are complex. So far, the finite element-based approach of full Navier-Stokes considering the Glen Law is the mainstream for predicting mountain glacier evolution, e.g., ELMER, Icetool (Jarosch, 2008; Zwinger and Moore, 2009), but these models also do not fully (or reasonably) account for all impact factors, especially for ice collapse in the frontal ice margin for land-terminating glaciers. Hence, it is difficult to robustly characterize the relationship between glacier dynamics and mechanical ablation, and also to fully evaluate its causes. We acknowledge that these causes can span one or more of full-thickness crevassing, points of structural weakness, highly dynamic hydraulic effects in the subglacial channels, undercutting, surface displacement, precipitation, and rapid thinning.

6. CONCLUSION

This study presents the geomorphological evolution of the terminus area of the HLG Glacier, SE TP, from October 17th 2017 to November 5th 2020 by applying UAV with SfM-MVS workflow. Using the orthophoto mosaics and DSMs, we investigated the mechanical ablation pattern at the terminus area of HLG Glacier by using geomorphic mapping for tracking the surface feature changes, DoD for evaluating the glacier snout ice loss, and DIC-FFT for extracting the displacement of the glacier. During the monitoring period, the HLG Glacier underwent continuous recession as evidenced by the changes in the area, terminus positions, and volume. Results suggest that the ice mass loss due to substantial frontal ice collapsing events exceeds the annual level of ice mass loss in the studied terminal area, which reveals that frontal ice collapsing events have a much more weighted influence on the mass balance of the HLG Glacier than previously understood.

The ablation pattern for the HLG Glacier terminus indicates that the glacier may to some extent be controlled by similar processes to those observed at lake-terminating glaciers. Specifically, the intensive water-glacier interactions near the subglacial channel outlet in the glacier terminus induce ice collapse events, indicating the terminus of HLG Glacier may be forced by the subglacial river. Moreover, the well-developed drainage networks in the glacier body facilitate ablation within the subglacial and englacial channels as a possible trigger for terminal ice collapse. The projection of the recession rate of the HLG Glacier may well be underestimated if based on surface mass balance alone, as the frontal ice collapsing might be more frequent and larger under the context of warming. Mechanical ablation is important at this site and could become even more significant to the ice loss of HLG Glacier with the continued warming. Therefore, this requires more future work regarding 3D modeling and sensitivity analysis to assess the impact of mechanical ablation on the glacier dynamics under the context of climate warming.

7. ACKNOWLEDGEMENTS

The authors greatly appreciate helpful and constructive suggestions and comments from the two anonymous referees, Prof. Ian S. Evans and Prof. Markus Stoffel (editor). This research was supported by the National Natural Science Foundation of China (Grand No. 41971078) and the Ph.D. faculty scholarship provided by the University of Nottingham Ningbo China. We also thank the Hailuogou Scenic Area Administration for the help in the field trips.

Supplemental files

This video was captured during the field trip of October 2017. The video showed an ice collapsing event that occurred in the subglacial channel outlet of HLG Glacier.

The link to the video is as follows:

https://v.youku.com/v_show/id_XMzA5MDg4NjExMg==.html?spm=a2hbt.13141534.app.5~5!2~5!2~5~5~5!2~5~5!2~5!2~5!2~5~5!11~A

References

Aizen, V.B., and Aizen, H.M. (1994). Regime and Mass-Energy Exchange of Subtropical Latitude Glaciers under Monsoon Climatic Conditions: Gongga Shan, Sichuan, China. Mountain Research and Development *14*, 101–118. https://doi.org/10.2307/3673794.

Ashraf, A., Roohi, R., Naz, R., and Mustafa, N. (2014). Monitoring cryosphere and associated flood hazards in high mountain ranges of Pakistan using remote sensing technique. Natural Hazards *73*, 933–949. https://doi.org/10.1007/s11069-014-1126-3.

Bash, E.A., Moorman, B.J., and Gunther, A. (2018). Detecting Short-Term Surface Melt on an Arctic Glacier Using UAV Surveys. Remote Sensing *10*, 1547. https://doi.org/10.3390/rs10101547.

Benn, D.I., and Åström, J.A. (2018). Calving glaciers and ice shelves. Advances in Physics: X *3*, 1513819. https://doi.org/10.1080/23746149.2018.1513819.

Berthier, E., and Toutin, T. (2008). SPOT5-HRS digital elevation models and the monitoring of glacier elevation changes in North-West Canada and South-East Alaska. Remote Sensing of Environment *112*, 2443–2454. https://doi.org/10.1016/j.rse.2007.11.004.

Bickel, V.T., Manconi, A., and Amann, F. (2018). Quantitative Assessment of Digital Image Correlation Methods to Detect and Monitor Surface Displacements of Large Slope Instabilities. Remote Sensing *10*, 865. https://doi.org/10.3390/rs10060865.

Bishop, M.P., Shroder, J.F., Haritashya, U.K., and Bulley, H.N.N. (2007). 25 Remote sensing and GIS for alpine glacier change detection in the Himalaya. In Developments in Earth Surface Processes, R. Baudo, G. Tartari, and E. Vuillermoz, eds. (Elsevier), pp. 209–234.

Carrivick, J.L., and Tweed, F.S. (2013a). Proglacial lakes: character, behaviour and geological importance. Quaternary Science Reviews *78*, 34–52. https://doi.org/10.1016/j.quascirev.2013.07.028.

Carrivick, J.L., and Tweed, F.S. (2013b). Proglacial lakes: character, behaviour and geological importance. Quaternary Science Reviews *78*, 34–52. https://doi.org/10.1016/j.quascirev.2013.07.028.

Chandler, B.M.P., Lovell, H., Boston, C.M., Lukas, S., Barr, I.D., Benediktsson, Í.Ö., Benn, D.I., Clark, C.D., Darvill, C.M., Evans, D.J.A., et al. (2018). Glacial geomorphological mapping: A review of approaches and frameworks for best practice. Earth-Science Reviews *185*, 806–846. https://doi.org/10.1016/j.earscirev.2018.07.015.

Che, Y., Wang, S., Yi, S., Wei, Y., and Cai, Y. (2020). Summer Mass Balance and Surface Velocity Derived by Unmanned Aerial Vehicle on Debris-Covered Region of Baishui River Glacier No. 1, Yulong Snow Mountain. Remote Sensing *12*, 3280. https://doi.org/10.3390/rs12203280.

Chen, J., Günther, F., Grosse, G., Liu, L., and Lin, H. (2018). Sentinel-1 InSAR Measurements of Elevation Changes over Yedoma Uplands on Sobo-Sise Island, Lena Delta. Remote Sensing *10*, 1152. https://doi.org/10.3390/rs10071152.

Di Rita, M., Fugazza, D., Belloni, V., Diolaiuti, G., Scaioni, M., and Crespi, M. (2020). GLACIER VOLUME CHANGE MONITORING FROM UAV OBSERVATIONS: ISSUES AND POTENTIALS OF STATE-OF-THE-ART TECHNIQUES. Int. Arch. Photogramm. Remote Sens. Spatial Inf. Sci. *XLIII-B2-2020*, 1041–1048. https://doi.org/10.5194/isprs-archives-XLIII-B2-2020-1041-2020.

Ding, Y., Liu, S., Li, J., and Shangguan, D. (2006). The retreat of glaciers in response to recent climate warming in western China. Annals of Glaciology *43*, 97–105. https://doi.org/10.3189/172756406781812005.

Egli, P.E., Belotti, B., Ouvry, B., Irving, J., and Lane, S.N. (2021). Subglacial Channels, Climate Warming, and Increasing Frequency of Alpine Glacier Snout Collapse. Geophysical Research Letters *48*, e2021GL096031. https://doi.org/10.1029/2021GL096031.

Falatkova, K., Šobr, M., Neureiter, A., Schöner, W., Janský, B., Häusler, H., Engel, Z., and Beneš, V. (2019). Development of proglacial lakes and evaluation of related outburst susceptibility at the Adygine ice-debris complex, northern Tien Shan. Earth Surface Dynamics *7*, 301–320. https://doi.org/10.5194/esurf-7-301-2019.

Fountain, A.G., and Walder, J.S. (1998). Water flow through temperate glaciers. Reviews of Geophysics *36*, 299–328. https://doi.org/10.1029/97RG03579.

Fu Y., Liu Q., Liu G., Zhang B., Zhang R., Cai J., Wang X., and Xiang W. (2021). Seasonal ice dynamics in the lower ablation zone of Dagongba Glacier, southeastern Tibetan Plateau, from multitemporal UAV images. Journal of Glaciology 1–15. https://doi.org/10.1017/jog.2021.123.

Fugazza, D., Scaioni, M., Corti, M., D'Agata, C., Azzoni, R.S., Cernuschi, M., Smiraglia, C., and Diolaiuti, G.A. (2018). Combination of UAV and terrestrial photogrammetry to assess rapid glacier evolution and map glacier hazards. Natural Hazards and Earth System Sciences *18*, 1055–1071. https://doi.org/10.5194/nhess-18-1055-2018.

Guizar-Sicairos, M., Thurman, S.T., and Fienup, J.R. (2008). Efficient subpixel image registration algorithms. Opt. Lett., OL *33*, 156–158. https://doi.org/10.1364/OL.33.000156.

Haresign, E.C. (2004). Glacio-limnological interactions at lake-calving glaciers. Thesis. University of St Andrews.

Heid, T., and Kääb, A. (2012). Evaluation of existing image matching methods for deriving glacier surface displacements globally from optical satellite imagery. Remote Sensing of Environment *118*, 339–355. https://doi.org/10.1016/j.rse.2011.11.024.

Hendrickx, H., Vivero, S., Cock, L.D., Wit, B.D., Maeyer, P.D., Lambiel, C., Delaloye, R., Nyssen, J., and Frankl, A. (2019). The reproducibility of SfM algorithms to produce detailed Digital Surface Models: the example of PhotoScan applied to a high-alpine rock glacier. Remote Sensing Letters *10*, 11–20. https://doi.org/10.1080/2150704X.2018.1519641.

Hooke, R.LeB. (1989). Englacial and Subglacial Hydrology: A Qualitative Review. Arctic and Alpine Research *21*, 221. https://doi.org/10.2307/1551561.

Immerzeel, W.W., Kraaijenbrink, P.D.A., Shea, J.M., Shrestha, A.B., Pellicciotti, F., Bierkens, M.F.P., and de Jong, S.M. (2014). High-resolution monitoring of Himalayan glacier dynamics using unmanned aerial vehicles. Remote Sensing of Environment *150*, 93–103. https://doi.org/10.1016/j.rse.2014.04.025.

James, L.A., Hodgson, M.E., Ghoshal, S., and Latiolais, M.M. (2012). Geomorphic change detection using historic maps and DEM differencing: The temporal dimension of geospatial analysis. Geomorphology *137*, 181–198. https://doi.org/10.1016/j.geomorph.2010.10.039.

Jarosch, A.H. (2008). Icetools: A full Stokes finite element model for glaciers. Computers & Geosciences *34*, 1005–1014. https://doi.org/10.1016/j.cageo.2007.06.012.

Kääb, A., Winsvold, S.H., Altena, B., Nuth, C., Nagler, T., and Wuite, J. (2016). Glacier Remote Sensing Using Sentinel-2. Part I: Radiometric and Geometric Performance, and Application to Ice Velocity. Remote Sensing *8*, 598. https://doi.org/10.3390/rs8070598.

Karimi, N., Sheshangosht, S., and Roozbahani, R. (2021). High-resolution monitoring of debris-covered glacier mass budget and flow velocity using repeated UAV photogrammetry in Iran. Geomorphology *389*, 107855. https://doi.org/10.1016/j.geomorph.2021.107855.

Kavanaugh, J.L., and Clarke, G.K.C. (2001). Abrupt glacier motion and reorganization of basal shear stress following the establishment of a connected drainage system. Journal of Glaciology *47*, 472–480. https://doi.org/10.3189/172756501781831972.

King, O., Dehecq, A., Quincey, D., and Carrivick, J. (2018). Contrasting geometric and dynamic evolution of lake and land-terminating glaciers in the central Himalaya. Global and Planetary Change *167*, 46–60. https://doi.org/10.1016/j.gloplacha.2018.05.006.

King, O., Bhattacharya, A., Bhambri, R., and Bolch, T. (2019). Glacial lakes exacerbate Himalayan glacier mass loss. Scientific Reports *9*, 18145. https://doi.org/10.1038/s41598-019-53733-x.

Kirkbride, M.P. (1993). The temporal significance of transitions from melting to calving termini at glaciers in the central Southern Alps of New Zealand. The Holocene *3*, 232–240. https://doi.org/10.1177/095968369300300305.

Kirkbride, M.P., and Warren, C.R. (1999). Tasman Glacier, New Zealand: 20th-century thinning and predicted calving retreat. Global and Planetary Change *22*, 11–28. https://doi.org/10.1016/S0921-8181(99)00021-1.

Li, S., Benson, C., Gens, R., and Lingle, C. (2008). Motion patterns of Nabesna Glacier (Alaska) revealed by interferometric SAR techniques. Remote Sensing of Environment *112*, 3628–3638. https://doi.org/10.1016/j.rse.2008.05.015.

Li, Z., He, Y., Jia, W., Pang, H., He, X., Wang, S., Zhang, N., Zhang, W., Liu, Q., and Xin, H. (2009). Changes in Hailuogou Glacier during the Recent 100 Years under Global Warming. Journal of Glaciology and Geocryology *31*, 75–81. .

Li, Z., He, Y., Yang, X., Theakstone, W.H., Jia, W., Pu, T., Liu, Q., He, X., Song, B., Zhang, N., et al. (2010). Changes of the Hailuogou glacier, Mt. Gongga, China, against the background of climate change during the Holocene. Quaternary International *218*, 166–175. https://doi.org/10.1016/j.quaint.2008.09.005.

Liu, Q., and Liu, S. (2010). Seasonal evolution of the englacial and subglacial drainage systems of a temperate glacier revealed by hydrological analysis. Sciences in Cold and Arid Regions *2*, 51–58. .

Liu, Q., and Liu, S. (2012). Tracer Test of Englacial and Subglacial Drainage System Evolution and a Case Study at Hailuogou Glacier. Journal of Glaciology and Geocryology *34*, 1207–1219. .

Liu, Q., and Zhang, Y. (2017). Studies on the Dynamics of Monsoonal Temperate Glacier in Mt. Gongga: a Review. Mountain Research *35*, 717–726. .

Liu, Q., Liu, S., Zhang, Y., Wang, X., Zhang, Y., Guo, W., and Xu, J. (2010). Recent shrinkage and hydrological response of Hailuogou glacier, a monsoon temperate glacier on the east slope of Mount Gongga, China. Journal of Glaciology *56*, 215–224. https://doi.org/10.3189/002214310791968520.

Liu, Q., Liu, S., and Cao, W. (2018). Seasonal Variation of Drainage System in the Lower Ablation Area of a Monsoonal Temperate Debris-Covered Glacier in Mt. Gongga, South-Eastern Tibet. Water *10*, 1050. https://doi.org/10.3390/w10081050.

Liu, Q., Mayer, C., Wang, X., Nie, Y., Wu, K., Wei, J., and Liu, S. (2020). Interannual flow dynamics driven by frontal retreat of a lake-terminating glacier in the Chinese Central Himalaya. Earth and Planetary Science Letters *546*, 116450. https://doi.org/10.1016/j.epsl.2020.116450.

Liu, S., Guo, W., Xu, J., ShangGuan, D., Wu, L., Yao, X., Zhao, J., Liu, Q., Jiang, Z., Li, P., et al. (2014). The Second Glacier Invertory Dataset of China (Version 1.0). Cold and Arid Regions Science Data Center https://doi.org/10.3972/glacier.001.2013.db.

Lu, R., and Gao, S. (1992). Debris Flow in the Ice Tongue Area of Hailuogou Glacier on the Eastern Slope of Mt.Gongga. Journal of Glaciology and Geocryology 73–80. .

Mair, D., Nienow, P., Willis, I., and Sharp, M. (2001). Spatial patterns of glacier motion during a high-velocity event: Haut Glacier d'Arolla, Switzerland. Journal of Glaciology *47*, 9–20. https://doi.org/10.3189/172756501781832412.

Mair, D., Nienow, P., Sharp, M., Wohlleben, T., and Willis, I. (2002a). Influence of subglacial drainage system evolution on glacier surface motion: Haut Glacier d'Arolla, Switzerland. Journal of Geophysical Research: Solid Earth *107*, EPM 8-1-EPM 8-13. https://doi.org/10.1029/2001JB000514.

Mair D., Willis I., Fischer U.H., Hubbard B., Nienow P., and Hubbard A. (2003). Hydrological controls on patterns of surface, internal and basal motion during three “spring events”: Haut Glacier d’Arolla, Switzerland. Journal of Glaciology *49*, 555–567. https://doi.org/10.3189/172756503781830467.

Mair, D.W.F., Sharp, M.J., and Willis, I.C. (2002b). Evidence for basal cavity opening from analysis of surface uplift during a high-velocity event: Haut Glacier d’Arolla, Switzerland. Journal of Glaciology *48*, 208–216. https://doi.org/10.3189/172756502781831502.

Maussion, F., Butenko, A., Champollion, N., Dusch, M., Eis, J., Fourteau, K., Gregor, P., Jarosch, A.H., Landmann, J., Oesterle, F., et al. (2019). The Open Global Glacier Model (OGGM) v1.1. Geoscientific Model Development *12*, 909–931. https://doi.org/10.5194/gmd-12-909-2019.

Mei, Z., Zhi-jiu, C., Geng-nian, L., Yi-xin, C., Zhen-yu, N., and Hai-rong, F. (2013). Formation and deformation of subglacier deposits of Hailuogou Glacier in Mt. Gongga, Southeastern Tibetan Plateau. Journal of Glaciology and Geocryology *35*, 1143–1155. .

Nye, J.F. (1951). The Flow of Glaciers and Ice-Sheets as a Problem in Plasticity. Proceedings of the Royal Society A: Mathematical, Physical and Engineering Sciences *207*, 554–572. https://doi.org/10.1098/rspa.1951.0140.

Pan, B.T., Zhang, G.L., Wang, J., Cao, B., Geng, H.P., Wang, J., Zhang, C., and Ji, Y.P. (2012). Glacier changes from 1966–2009 in the Gongga Mountains, on the south-eastern margin of the Qinghai-Tibetan Plateau and their climatic forcing. The Cryosphere *6*, 1087–1101. https://doi.org/10.5194/tc-6-1087-2012.

Rossini, M., Di Mauro, B., Garzonio, R., Baccolo, G., Cavallini, G., Mattavelli, M., De Amicis, M., and Colombo, R. (2018a). Rapid melting dynamics of an alpine glacier with repeated UAV photogrammetry. Geomorphology *304*, 159–172. https://doi.org/10.1016/j.geomorph.2017.12.039.

Rossini, M., Di Mauro, B., Garzonio, R., Baccolo, G., Cavallini, G., Mattavelli, M., De Amicis, M., and Colombo, R. (2018b). Rapid melting dynamics of an alpine glacier with repeated UAV photogrammetry. Geomorphology *304*, 159–172. https://doi.org/10.1016/j.geomorph.2017.12.039.

Rusnák, M., Sládek, J., Kidová, A., and Lehotský, M. (2018). Template for high-resolution river landscape mapping using UAV technology. Measurement *115*, 139–151. https://doi.org/10.1016/j.measurement.2017.10.023.

Ryan, J.C., Hubbard, A.L., Box, J.E., Todd, J., Christoffersen, P., Carr, J.R., Holt, T.O., and Snooke, N. (2015). UAV photogrammetry and structure from motion to assess calving dynamics at Store Glacier, a large outlet draining the Greenland ice sheet. The Cryosphere *9*, 1–11. https://doi.org/10.5194/tc-9-1-2015.

Sakai, A. (2012). Glacial Lakes in the Himalayas: A Review on Formation and Expansion Processes. 8. .

Sakai, A., and Fujita, K. (2010). Formation conditions of supraglacial lakes on debris-covered glaciers in the Himalaya. Journal of Glaciology *56*, 177–181. https://doi.org/10.3189/002214310791190785.

Sakai, A., Nishimura, K., Kadota, T., and Takeuchi, N. (2009). Onset of calving at supraglacial lakes on debris-covered glaciers of the Nepal Himalaya. Journal of Glaciology *55*, 909–917. https://doi.org/10.3189/002214309790152555.

Smith, M.W., Carrivick, J.L., and Quincey, D.J. (2016). Structure from motion photogrammetry in physical geography. Progress in Physical Geography *40*, 247–275. https://doi.org/10.1177/0309133315615805.

Strozzi, T., Luckman, A., Murray, T., Wegmuller, U., and Werner, C.L. (2002). Glacier motion estimation using SAR offset-tracking procedures. IEEE Transactions on Geoscience and Remote Sensing *40*, 2384–2391. https://doi.org/10.1109/TGRS.2002.805079.

Stucky de Quay, G., Roberts, G.G., Rood, D.H., and Fernandes, V.M. (2019). Holocene uplift and rapid fluvial erosion of Iceland: A record of post-glacial landscape evolution. Earth and Planetary Science Letters *505*, 118–130. https://doi.org/10.1016/j.epsl.2018.10.026.

Su, Z., and Shi, Y. (2000). Response of Monsoonal Temperature Glacier in China to Global Warming Since the Little Ice Age. Journal of Glaciology and Geocryology *22*, 223–229. .

Sun, J., Zhou, T., Liu, M., Chen, Y., Shang, H., Zhu, L., Shedayi, A.A., Yu, H., Cheng, G., Liu, G., et al. (2018). Linkages of the dynamics of glaciers and lakes with the climate elements over the Tibetan Plateau. Earth-Science Reviews *185*, 308–324. https://doi.org/10.1016/j.earscirev.2018.06.012.

Thorsteinsson, T., Raymond, C.F., Gudmundsson, G.H., Bindschadler, R.A., Vornberger, P., and Joughin, I. (2003). Bed topography and lubrication inferred from surface measurements on fast-flowing ice streams. Journal of Glaciology *49*, 481–490. https://doi.org/10.3189/172756503781830502.

Verhoeven, G. (2011). Taking computer vision aloft – archaeological three-dimensional reconstructions from aerial photographs with photoscan. Archaeological Prospection *18*, 67–73. https://doi.org/10.1002/arp.399.

Walder, J.S. (2010). Röthlisberger channel theory: its origins and consequences. Journal of Glaciology *56*, 1079–1086. https://doi.org/10.3189/002214311796406031.

Wang, J., Pan, B., Zhang, G., Cui, H., Cao, B., and Geng, H. (2013). Late Quaternary glacial chronology on the eastern slope of Gongga Mountain, eastern Tibetan Plateau, China. Sci. China Earth Sci. *56*, 354–365. https://doi.org/10.1007/s11430-012-4514-0.

Wheaton, J.M., Brasington, J., Darby, S.E., and Sear, D.A. (2009). Accounting for uncertainty in DEMs from repeat topographic surveys: improved sediment budgets. Earth Surf. Process. Landforms n/a-n/a. https://doi.org/10.1002/esp.1886.

Wu, K., Liu, S., Zhu, Y., Liu, Q., and Jiang, Z. (2020). Dynamics of glacier surface velocity and ice thickness for maritime glaciers in the southeastern Tibetan Plateau. Journal of Hydrology *590*, 125527. https://doi.org/10.1016/j.jhydrol.2020.125527.

Xu, X., and Yi, C. (2017). Timing and configuration of the Gongga II glaciation in the Hailuogou valley, eastern Tibetan Plateau: A glacier-climate modeling method. Quaternary International *444*, 151–156. https://doi.org/10.1016/j.quaint.2017.01.011.

Yang, W., Guo, X., Yao, T., Zhu, M., and Wang, Y. (2016). Recent accelerating mass loss of southeast Tibetan glaciers and the relationship with changes in macroscale atmospheric circulations. Clim Dyn *47*, 805–815. https://doi.org/10.1007/s00382-015-2872-y.

Yang, W., Zhao, C., Westoby, M., Yao, T., Wang, Y., Pellicciotti, F., Zhou, J., He, Z., and Miles, E. (2020). Seasonal Dynamics of a Temperate Tibetan Glacier Revealed by High-Resolution UAV Photogrammetry and In Situ Measurements. Remote Sensing *12*, 2389. https://doi.org/10.3390/rs12152389.

Zhang, G., Pan, B., Cao, B., Wang, J., Cui, H., and Cao, X. (2015). Elevation changes measured during 1966–2010 on the monsoonal temperate glaciers' ablation region, Gongga Mountains, China. Quaternary International *371*, 49–57. https://doi.org/10.1016/j.quaint.2015.03.055.

Zhang, Y., Fujita, K., Liu, S., Liu, Q., and Wang, X. (2010). Multi-decadal ice-velocity and elevation changes of a monsoonal maritime glacier: Hailuogou glacier, China. Journal of Glaciology *56*, 65–74. https://doi.org/10.3189/002214310791190884.

Zhang, Y., Fujita, K., Liu, S., Liu, Q., and Nuimura, T. (2011). Distribution of debris thickness and its effect on ice melt at Hailuogou glacier, southeastern Tibetan Plateau, using in situ surveys and ASTER imagery. Journal of Glaciology *57*, 1147–1157. https://doi.org/10.3189/002214311798843331.

Zhang, Y., Hirabayashi, Y., and Liu, S. (2012). Catchment-scale reconstruction of glacier mass balance using observations and global climate data: Case study of the Hailuogou catchment, south-eastern Tibetan Plateau. Journal of Hydrology *444–445*, 146–160. https://doi.org/10.1016/j.jhydrol.2012.04.014.

Zhang, Y., Hirabayashi, Y., Fujita, K., Liu, S., and Liu, Q. (2016). Heterogeneity in supraglacial debris thickness and its role in glacier mass changes of the Mount Gongga. Sci. China Earth Sci. *59*, 170–184. https://doi.org/10.1007/s11430-015-5118-2.

Zhang, Y., Liu, S., and Wang, X. (2018). A dataset of spatial distribution of debris cover on Hailuogou Glacier of Mount Gongga in 2009. Science Data Bank *3*. .

Zhong, Y., Liu, Q., Westoby, M., Nie, Y., Pellicciotti, F., Zhang, B., Cai, J., Liu, G., Liao, H., and Lu, X. (2021). Intensified paraglacial slope failures due to accelerating downwasting of a temperate glacier in Mt. Gongga, Southeastern Tibet Plateau. Earth Surface Dynamics Discussions 1–31. https://doi.org/10.5194/esurf-2021-18.

Zwinger, T., and Moore, J.C. (2009). Diagnostic and prognostic simulations with a full Stokes model accounting for superimposed ice of Midtre Lovénbreen, Svalbard. The Cryosphere *3*, 217–229. https://doi.org/10.5194/tc-3-217-2009.